Geochemical Perspectives Letters
EAG

Published by the European Association of Geochemistry

Testing *ab initio* garnet-clinopyroxene Ca-isotope fractionation models with natural data

J. Munro[1]*, J.C. Lassiter[1], J.D. Barnes[1], A.M. Satkoski[1]

OPEN ACCESS
https://doi.org/10.7185/geochemlet.2549

Abstract

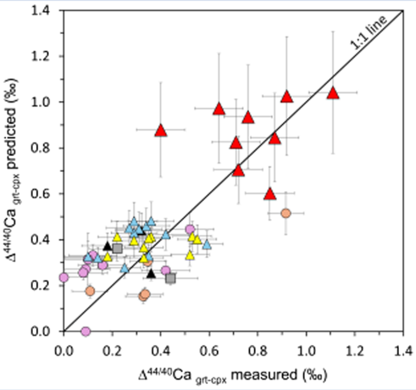

Calcium stable isotope variations help track processes from melt generation to crustal recycling in the mantle, but applying this system requires understanding of inter-mineral and mineral-melt isotopic fractionation. Density functional theory (DFT) models have been used to constrain Ca-isotope fractionation between garnet and clinopyroxene as a function of temperature, pressure, and composition, because garnet can strongly fractionate Ca. However, experimental and empirical data to test DFT predictions for equilibrium $\Delta^{44/40}Ca_{grt\text{-}cpx}$ remain limited. We measured $\delta^{44/40}Ca$ values of clinopyroxene and garnet from eclogite xenoliths in the Navajo Volcanic Field, Colorado Plateau (USA). Combining these low-temperature samples with higher-temperature literature data, we find $\Delta^{44/40}Ca_{grt\text{-}cpx}$ is correlated with $10^6/T^2$ ($\Delta^{44/40}Ca_{grt\text{-}cpx} = 0.63 \times 10^6/T^2$). No correlations were found with mineral composition after correcting for temperature, and pressure is not expected to have a significant effect. To first order, DFT model predictions agree well with observed trends in natural samples.

Received 7 August 2025 | Accepted 6 November 2025 | Published 4 December 2025

Introduction

Mantle peridotites exhibit limited variation in $\delta^{44/40}Ca$ ($\delta^{44/40}Ca = [(^{44}Ca/^{40}Ca)_{sample}/(^{44}Ca/^{40}Ca)_{SRM915a} - 1] \times 1000$; *e.g.*, Dai *et al.*, 2020), but Ca isotopes are significantly fractionated during surface processes (He *et al.*, 2023 and references therein). Consequently, Ca isotopes have been utilised as tracers for recycled material and proxies for carbonate cycling in the mantle, especially when considering low-$\delta^{44/40}Ca$ basalts or carbonatites (Kang *et al.*, 2016, 2017; Chen *et al.*, 2023; Li *et al.*, 2024; Zhu *et al.*, 2025). However, this view is challenged by a broad negative correlation between $\delta^{44/40}Ca$ and La/Lu observed in mid-ocean ridge basalts (MORB) and ocean island basalts (OIB; Eriksen and Jacobsen, 2022 and references therein). Because garnet strongly fractionates both Ca isotopes and heavy REE, this correlation may reflect isotopic fractionation during melting of garnet-bearing lithologies (Eriksen *et al.*, 2024). In contrast, clinopyroxene-melt fractionation produces melts with $\delta^{44/40}Ca$ values only <0.1 ‰ lower than spinel peridotites (Eriksen and Jacobsen, 2022; Chen *et al.*, 2024). Parameterising garnet-clinopyroxene fractionation is therefore necessary to model the effects of melting of garnet-bearing sources on melt $\delta^{44/40}Ca$, better enabling us to distinguish contributions from equilibrium melting, sedimentary recycling and disequilibrium processes on the $\delta^{44/40}Ca$ of xenoliths and mantle-derived melts.

To characterise the behaviour of calcium isotopes during equilibrium fractionation, studies have focused on identifying the primary factors, such as temperature (Antonelli *et al.*, 2019; Li *et al.*, 2022), pressure (Chen *et al.*, 2020; Li *et al.*, 2022) and mineral composition (Antonelli *et al.*, 2019; Chen *et al.*, 2020), that control inter-mineral or mineral-melt isotopic fractionation. Modelling the effects of these parameters is essential to constrain the $\delta^{44/40}Ca$ variation generated during igneous and metamorphic processes under isotopic equilibrium (Li *et al.*, 2025). However, to date, most studies have relied on theoretical *ab initio* modelling (Antonelli *et al.*, 2019; Chen *et al.*, 2020; Li *et al.*, 2022; Xiao *et al.*, 2022), with limited use of natural or experimental samples to validate model predictions (Smart *et al.*, 2021; Li *et al.*, 2022, 2025). Furthermore, the few natural samples analysed have predominantly come from South African kimberlite localities (Roberts Victor, Chen *et al.*, 2020; Li *et al.*, 2022; Bellsbank, Smart *et al.*, 2021; and Premier, Tappe *et al.*, 2021), which equilibrated at high temperatures (>800 °C). Hence, the temperature dependence of Ca-isotope fractionation has not yet been adequately tested.

We present new mineral $\delta^{44/40}Ca$ data for a suite of low-temperature eclogites from the Navajo Volcanic Field (NVF) in the Colorado Plateau, USA. These results are combined with existing garnet and clinopyroxene $\delta^{44/40}Ca$ from natural samples to test first-principles $\delta^{44/40}Ca$ fractionation models. We evaluate the proposed factors controlling garnet-clinopyroxene Ca-isotope fractionation, and consider the implications for $\delta^{44/40}Ca$ fractionation during partial melting.

Sample Description Results

Eclogitic xenoliths ($n = 9$) from Garnet Ridge ultramafic diatreme were selected from the NVF xenolith collection at the University of Texas at Austin (UT-Austin). They are subrounded nodules

1. Department of Earth and Planetary Sciences, University of Texas at Austin, Austin, Texas, United States of America
* Corresponding author (email: joshua.munro@utexas.edu)

approximately 2 to 4.5 cm in diameter, dominated by jadeite-rich pyroxene, almandine-rich garnet, with lawsonite and zoisite (Table S-1). Garnet and clinopyroxene major element compositions were determined by electron microprobe (Table S-2) for Mg-Fe garnet-clinopyroxene thermometry. Calcium isotope data were collected at UT-Austin. See Supplementary Information for method details. Garnet $\delta^{44/40}$Ca values range from 1.54 to 1.98 ‰ and pyroxenes vary from 0.76 to 1.21 ‰, with $\delta^{44/40}$Ca fractionation ($\Delta^{44/40}Ca_{grt\text{-}cpx} = \delta^{44/40}Ca_{garnet} - \delta^{44/40}Ca_{clinopyroxene}$) values of 0.64 to 1.11 ‰ (Table S-3).

Discussion

Comparison of natural data to Ca-isotope fractionation models. Density functional theory (DFT) models predict that Ca-isotope fractionation is primarily controlled by Ca-O bond strength, with vibrational frequencies and force constants influencing bond stiffness and thus isotope partitioning (Schauble, 2004; Antonelli *et al.*, 2019; Li *et al.*, 2022; Xiao *et al.*, 2022). Equilibrium fractionation arises from vibrational zero-point energy differences and partition functions, in which heavier isotopes preferentially occupy sites with stiffer bonds (*e.g.*, Schauble, 2004). Fractionation is proportional to $1/T^2$ because increasing temperature results in a smaller difference in vibrational energy between two phases. Because mineral composition variation affects lattice structure, this also influences Ca-O bond length and $\Delta^{44/40}Ca_{grt\text{-}cpx}$ (*e.g.*, Antonelli *et al.*, 2019). This effect is predicted to be greater in garnet than in clinopyroxene because the garnet lattice is more rigid and therefore more affected by cation substitutions than the comparatively flexible pyroxene lattice (Antonelli *et al.*, 2019; Li *et al.*, 2022).

The accuracy of DFT models depends on theoretical assumptions, such as the choice of vibration energy model or functional (Local Density Approximation *vs.* Generalised Gradient Approximation), lattice framework chosen, choice of mineral endmembers, and parameters chosen for adjustment (*e.g.*, composition or pressure; Li *et al.*, 2025). Due to computational limitations, models are generally run for compositional endmembers rather than complex solid solutions. Uncertainties in vibrational frequency inputs and use of different approaches or software can introduce systematic errors (Li *et al.*, 2025), which may produce discrepancies between empirical data and *ab initio* predictions. Systematic errors within approaches may be cancelled out when using the same models for a mineral pair, but unpredictable errors may occur when approaches from different papers are combined (Li *et al.*, 2025).

To test whether first-principles models accurately predict isotopic fractionation in natural samples, we present $\Delta^{44/40}Ca_{grt\text{-}cpx}$ from this and previous studies against $10^6/T^2$ (Fig. 1). To ensure estimated temperatures are internally consistent, we apply the same garnet-clinopyroxene Mg-Fe thermometer procedure to all NVF and literature samples (see Supplementary Information). The natural data are compared to DFT models from Antonelli *et al.* (2019), Li *et al.* (2022) and Xiao *et al.* (2022). The shaded regions show the model ranges for: Antonelli *et al.* (2019), where garnet almandine-grossular-pyrope composition is varied and clinopyroxene is fixed as diopside; Li *et al.* (2022), bound by their 0 and 10 GPa pyrope-diopside models; and Xiao *et al.* (2022), in which the garnet is fixed as almandine, and jadeite type changes with variable Na + Al substitution for Ca + Mg.

The weighted regression of all the natural data yields the following line:

$$\Delta^{44/40}Ca_{grt\text{-}cpx} = 1.44(\pm 0.15) \times 10^6/T^2 - 0.51(\pm 0.09), \qquad \text{Eq. 1}$$

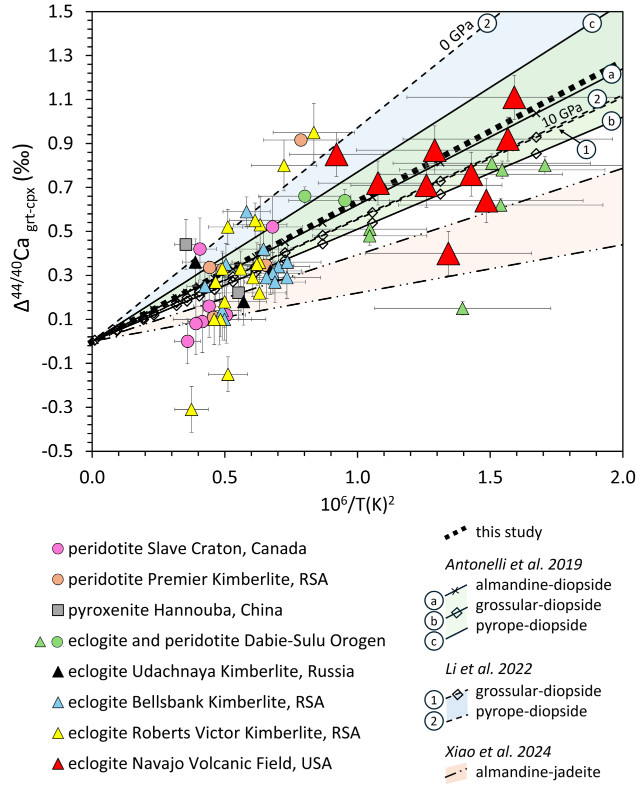

Figure 1 $\Delta^{44/40}Ca_{grt\text{-}cpx}$ plotted against $1/T^2$ for the samples in this study and previous work (see text). Natural data for eclogites (triangles), peridotites (circles) and pyroxenites (squares) are compared to DFT models by Antonelli *et al.* (2019), Li *et al.* (2022) and Xiao *et al.* (2022). All temperatures recalculated following the protocol described in Supplementary Information. Error bars represent 2 s.e., some are smaller than symbols. The Li *et al.* (2022) grossular-diopside and 10 GPa pyrope-diopside lines overlap.

with a mean squared weighted deviation (MSWD) of 7.5 ($n = 65$). The slope of this fractionation line is significantly greater than DFT predictions, and the intercept is non-zero, inconsistent with models. Li *et al.* (2022) noted that Type II Roberts Victor samples ('unmetasomatised') form a steeply dipping array (increasing $\Delta^{44/40}Ca_{grt\text{-}cpx}$ with $10^6/T^2$) and contain samples with $\Delta^{44/40}Ca_{grt\text{-}cpx} < 0$, inconsistent with model predictions. It is unclear whether this is a disequilibrium process (Antonelli *et al.*, 2019), pressure effect (Chen *et al.*, 2020), due to jadeite/high-pressure garnet that have since destabilised (Li *et al.*, 2022), or a mixture of processes. Because the Ca-isotope equilibrium of those samples is debated, they are excluded, reducing the MSWD to 6.4 and bringing the regression more in line with predictions (see Eq. S-2).

Additionally, we note that the only *in situ* samples are from the Dabie-Sulu Orogen, which has undergone slow exhumation (Hacker *et al.*, 2006). Mg-Fe diffusion is more rapid and continues to lower temperatures than Ca diffusion (Ganguly, 2010). Hence, these slowly-cooled samples are expected to have $T_{Mg\text{-}Fe}$ less than T_{Ca}. Because the $T_{Mg\text{-}Fe}$ is expected to not be in equilibrium with $\Delta^{44/40}Ca_{grt\text{-}cpx}$, these samples are also not suited to this analysis. Removing Dabie-Sulu samples from the regression improves the MSWD to 5.7 (Eq. S-3). A final consideration is the non-zero intercept – DFT modelling and thermodynamics predict that $\Delta^{44/40}Ca_{grt\text{-}cpx}$ converges to 0 as T approaches infinity (Schauble, 2004). Because no sign reversal is anticipated for Ca-isotope fractionation of garnet and clinopyroxene, the regression is forced to the intercept. The heavy dashed line is the weighted regression of all natural data, excluding Dabie-Sulu and Type II Roberts Victor (Fig. 1). The revised empirical, temperature-dependent model is now:

$$\Delta^{44/40}Ca_{grt\text{-}cpx} = 0.63(\pm 0.03) \times 10^6/T^2. \qquad \text{Eq. 2}$$

This model is consistent with DFT predictions, as the slope is within the range of Antonelli *et al.* (2019) and slightly higher than the slopes of 0.567 from Huang *et al.* (2019) and 0.52 from Li *et al.* (2025). Increasing $\Delta^{44/40}Ca_{grt\text{-}cpx}$ fractionation is correlated with decreasing temperature (increasing $10^6/T^2$; MSWD = 6.8, $n = 49$, $p < 0.001$). The NVF eclogites, which have lower temperature estimates (~500 to 800 °C; Table S-5) than most literature samples (~900 to 1200 °C), have higher $\Delta^{44/40}Ca_{grt\text{-}cpx}$, as predicted.

By using the average garnet composition for all samples ($Py_{47}Alm_{34}Grs_{18}$) to linearly mix the Antonelli *et al.* (2019) pyrope-, almandine- and grossular-diopside models, one obtains a model indistinguishable from Equation 2 (slope = 0.64). Hence, to a first order, DFT modelling accurately predicts natural observations.

Constraining controls on natural $\Delta^{44/40}Ca_{grt\text{-}cpx}$ variability. Despite the similarity between the empirical and DFT models, the natural samples show significant scatter from the regression (Fig. 1 and Fig. S-5), which may be due to analytical error, or reflect the influence of factors such as pressure (Chen *et al.*, 2020), garnet composition (Chen *et al.*, 2020; Li *et al.*, 2022), pyroxene composition (Wang *et al.*, 2019; Li *et al.*, 2022; Xiao *et al.*, 2022), or disequilibrium effects (Antonelli *et al.*, 2019). To test the influence of these parameters, the departure of natural samples from the regression is quantified using residuals (measured $\Delta^{44/40}Ca_{grt\text{-}cpx}$ − predicted $\Delta^{44/40}Ca_{grt\text{-}cpx}$). The linear regression (Eq. 2) is used to calculate the predicted $\Delta^{44/40}Ca_{grt\text{-}cpx}$ from temperature estimates for each sample, and the residuals are then compared to compositional parameters and pressure estimates (Fig. 2) to assess correlations.

First, though, it is worth testing whether the scatter is due to random errors. The residuals are compared to the normal distribution of expected errors from thermometric uncertainty, isotopic measurement error and error in the linear regression (average total 2σ = 0.14 ‰; Fig. 3). The true residual 2σ is 0.34 ‰. Hence, while some departures may be due to uncertainty in Mg-Fe exchange thermometry and measured $\Delta^{44/40}Ca_{grt\text{-}cpx}$, most scatter is unaccounted for.

Varying garnet composition from grossular to almandine to pyrope is predicted to increase $\Delta^{44/40}Ca_{grt\text{-}cpx}$ (Antonelli *et al.*, 2019) because these cation substitutions decrease the Ca-O bond length, but we do not observe correlations between residuals and garnet almandine, grossular, or pyrope content (grossular shown; Fig. 2). However, at high temperatures (>1000 K) the compositional effect is expected to be <0.2 ‰ (*e.g.*, Li *et al.*, 2025), similar to the propagated measurement errors, and so compositional effects may not be easily observable given other sources of scatter. It is clear, however, that for a given temperature, $\Delta^{44/40}Ca_{grt\text{-}cpx}$ varies more than is predicted for compositional variation (Fig. 2).

Due to similar ionic sizes, Mg-Fe substitution does not significantly alter the pyroxene lattice size. Hence, no Ca-O bond length change (or $\Delta^{44/40}Ca_{grt\text{-}cpx}$ effect) is expected. Consistent with this, there is no clear correlation between residuals and diopside content, as noted by Li *et al.* (2025). A correlation between $\Delta^{44/40}Ca_{grt\text{-}cpx}$ and jadeite content was previously reported for Dabie-Sulu eclogites (Wang *et al.*, 2019), and DFT modelling by Xiao *et al.* (2022) predicts $\Delta^{44/40}Ca_{grt\text{-}cpx}$ changes depending on how Na + Al is substituted in jadeite. However,

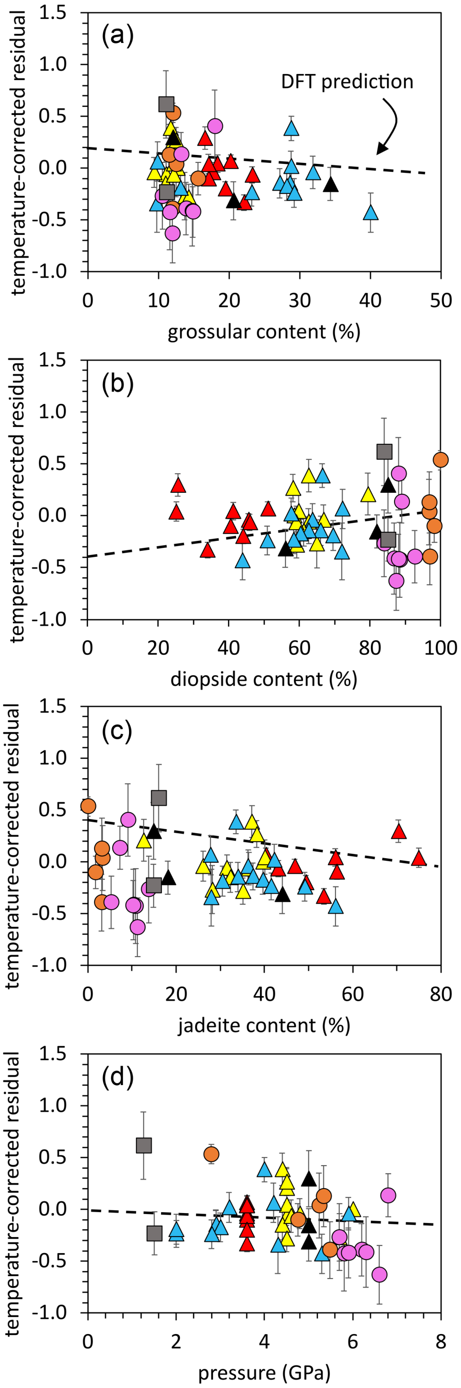

Figure 2 Plots of temperature-corrected $\Delta^{44/40}Ca_{grt\text{-}cpx}$ residuals against **(a)** garnet grossular content, **(b)** pyroxene diopside content, **(c)** pyroxene jadeite content, and **(d)** pressure estimates. Symbols as for Figure 1.

neither Chen *et al.* (2020) nor Smart *et al.* (2021) observed $\Delta^{44/40}Ca_{grt\text{-}cpx}$ correlations with jadeite content in mantle eclogites. Similarly, no correlation is seen with the global dataset of $\Delta^{44/40}Ca_{grt\text{-}cpx}$ residuals and jadeite content (Fig. 2). Therefore, clinopyroxene composition does not detectably influence $\Delta^{44/40}Ca_{grt\text{-}cpx}$.

Clinopyroxene lattice structure is more compressible than that of garnet and is predicted to have shorter Ca-O bond lengths at greater pressures, increasing uptake of ^{44}Ca into clinopyroxene and reducing $\Delta^{44/40}Ca_{grt\text{-}cpx}$. Chen *et al.* (2020) determined pressure estimates and $\Delta^{44/40}Ca_{grt\text{-}cpx}$ for Roberts

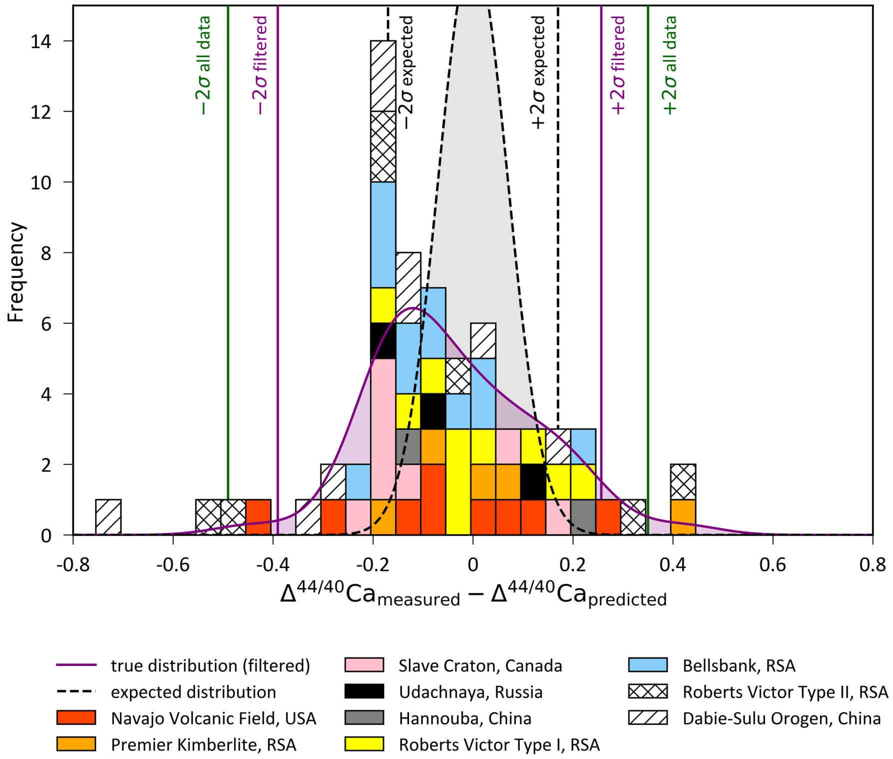

Figure 3 Histogram of $\Delta^{44/40}Ca_{grt\text{-}cpx}$ residuals, and error distribution expected from the predicted $\Delta^{44/40}Ca_{grt\text{-}cpx}$ and $1/T^2$ uncertainty (dashed lines) compared to the actual distribution of filtered residuals (purple lines; excluded Dabie-Sulu or Roberts Victor Type II).

Victor eclogites to infer that Ca fractionation decreases by 0.3 ‰ over 3 to 4.5 GPa (1000 K). However, *ab initio* modelling by Li *et al.* (2022, 2025) suggests garnet and clinopyroxene lattices are equally affected by pressure, yielding pressure-induced $\Delta^{44/40}Ca_{grt\text{-}cpx}$ variation of <0.05 ‰ at 1000 K. Significant pressure effects do occur when garnet Ca concentration is very low (<1 wt. %, pyrope-diopside models; Li *et al.*, 2022), but most natural samples examined have Ca as a major element (up to 20 wt. %). We do not observe a correlation between the $\Delta^{44/40}Ca_{grt\text{-}cpx}$ residuals of natural samples and estimated published pressures (Fig. 2). It is not possible to clearly assess the pressure effect with current data because the pressure estimates are based on the Mg-Fe thermometry, and *vice versa*, but recent models predict small effects.

Some unexplained scatter is likely due to disequilibrium (*e.g.*, subsolidus Ca-isotope diffusion) or a mismatch between Ca and Mg-Fe closure temperatures. Overall, no clear signs of disequilibrium were observed when examining garnet-clinopyroxene Mg, Ti and REE partitioning (see Supplementary Information). Because rapid Mg-Fe diffusion continues to lower temperatures than Ca, where samples cooled slowly as for *in situ* Dabie-Sulu samples, the Mg-Fe temperature estimates are likely lower than the Ca-isotope closure temperature. This would result in overestimation of the predicted $\Delta^{44/40}Ca_{grt\text{-}cpx}$ so that residuals would be shifted to negative values. If the sample was rapidly heated, *i.e.* during eruption, Mg-Fe temperature may be reset to higher temperatures, whereas the Ca-isotope temperatures may remain unperturbed, producing the opposite shift in residuals. There is evidence of temperature inconsistencies when REE and Mg-Fe thermometry are compared (Fig. S-3), and this may be a major contributor to the broader than expected error distribution. Unfortunately, no garnet-clinopyroxene Ca geothermometer exists, but the Mg-Fe thermometers are the most accessible and widely used method, generally producing a reasonable approximation to the Ca-isotope temperature for rapidly exhumed samples.

Although disequilibrium processes (*e.g.*, diffusion) likely affect some samples, most natural samples are close to equilibrium, within the current ability to determine temperature and $\Delta^{44/40}Ca_{grt\text{-}cpx}$. General disequilibrium processes are unlikely to dominate during processes such as melt generation.

Ca-isotope variation in basalts. Ocean island basalts span a wider $\delta^{44/40}Ca$ range and extend to lower values than MORB (Eriksen and Jacobsen, 2022). There is debate whether Ca-isotope variations in MORB and OIB primarily reflect variations in source composition (*e.g.*, incorporation of recycled components; Huang *et al.*, 2011), isotopic fractionation variations due to melting of garnet-rich and garnet-poor lithologies (*e.g.*, Dai *et al.*, 2020), or disequilibrium fractionation during melt generation (*e.g.*, kinetic effects; Antonelli *et al.*, 2019; Li *et al.*, 2025). Eriksen *et al.* (2024) and Eriksen and Jacobsen (2022) suggest the OIB $\delta^{44/40}Ca$ correlation with La/Lu reflects mixing of melts derived from garnet-rich and garnet-poor lithologies, but also suggest involvement of recycling and source enrichment. Whereas previous studies used DFT models to constrain inter-mineral and mineral-melt isotopic fractionation, our study provides independent confirmation of DFT estimates using natural samples.

Using the clinopyroxene-melt Ca-isotope fractionation of Li *et al.* (2025) and Equation 2, we model the $\delta^{44/40}Ca$ range likely generated during melting of spinel peridotite, garnet peridotite, and garnet-dominated lithologies (*e.g.*, garnetite or rodingite). The observed OIB $\delta^{44/40}Ca$ range is unlikely to simply reflect mixing of melts from garnet and spinel peridotite, assuming a starting peridotite composition of ~0.94 ‰ (Fig. 4). Assuming equal modal abundances of garnet and clinopyroxene, results show that partial melting of garnet peridotite (or eclogite) does not generate melts with $\delta^{44/40}Ca < 0.78$ ‰. Even melting of pure

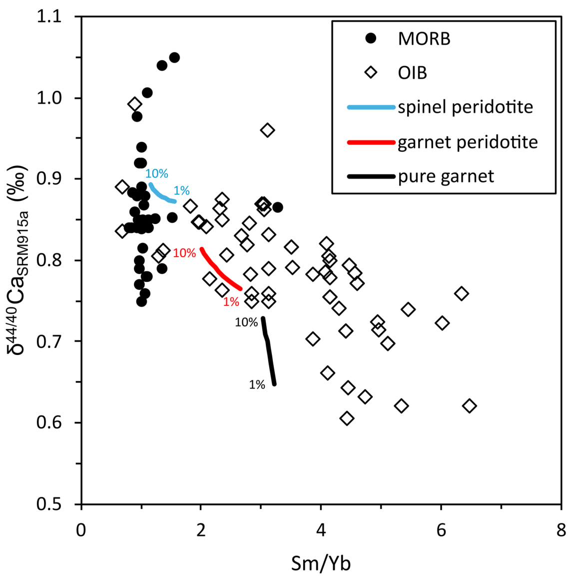

Figure 4 Comparison of $\delta^{44/40}$Ca *versus* Sm/Yb for MORB (Erikson and Jacobsen, 2022) and OIB (Eriksen *et al.*, 2024). Lines represent batch melting of a spinel peridotite, garnet peridotite or pure garnet source, with 1 to 10 % partial melting.

garnet lithologies cannot generate melts with $\delta^{44/40}$Ca < 0.69 ‰. Thus, the lowest observed OIB $\delta^{44/40}$Ca (high La/Lu and Sm/Yb) likely derive from anomalously low-$\delta^{44/40}$Ca sources, possibly due to incorporation of recycled carbonates or prior metasomatism by melts derived from garnet-bearing sources. Additionally, the global correlation observed between $\delta^{44/40}$Ca and La/Lu and Sr and Nd isotopes (Eriksen *et al.*, 2024) suggests that variation in source composition, rather than disequilibrium fractionation, is responsible for generating the large OIB $\delta^{44/40}$Ca range.

Acknowledgements

The authors are grateful to D. Smith for curating the UT-Austin NVF collection and sharing samples, the Navajo Nation for permission to collect on their land, K.S. Befus and A.V. Mott for assistance in obtaining electron microprobe analyses, and C. Sun for valuable discussions. The efficient editorial handling by R. Tartèse and constructive reviews of E. Schauble and an anonymous reviewer are greatly appreciated. This work was supported by a National Science Foundation (NSF) grant to JDB and JCL (#2234385) and Geological Society of America (GSA) Lipman Student Research Grant to JM.

Editor: Romain Tartèse

Additional Information

Supplementary Information accompanies this letter at https://www.geochemicalperspectivesletters.org/article2549.

Cite this letter as: Munro, J., Lassiter, J.C., Barnes, J.D., Satkoski, A.M. (2025) Testing *ab initio* garnet-clinopyroxene Ca-isotope fractionation models with natural data. *Geochem. Persp. Let.* 38, 11–16. https://doi.org/10.7185/geochemlet.2549

References

Antonelli, M.A., Schiller, M., Schauble, E.A., Mittal, T., DePaolo, D.J., Chacko, T., Grew, E.S., Tripoli, B. (2019) Kinetic and equilibrium Ca isotope effects in high-T rocks and minerals. *Earth and Planetary Science Letters* 517, 71–82. https://doi.org/10.1016/j.epsl.2019.04.013

Chen, C., Huang, J.-X., Foley, S.F., Wang, Z., Moynier, F., Liu, Y., Dai, W., Li, M. (2020) Compositional and pressure controls on calcium and magnesium isotope fractionation in magmatic systems. *Geochimica et Cosmochimica Acta* 290, 257–270. https://doi.org/10.1016/j.gca.2020.09.006

Chen, C., Foley, S.F., Tappe, S., Ren, H., Feng, L., Liu, Y. (2024) Calcium isotopes track volatile components in the mantle sources of alkaline rocks and associated carbonatites. *Earth and Planetary Science Letters* 625, 118489. https://doi.org/10.1016/j.epsl.2023.118489

Chen, Q., Zhou, M.-F., Xia, X.-P., Liu, P.-P. (2023) Li and O isotopes of mantle xenoliths from deep fault-related Cenozoic basalts in eastern China: The role of subducted components in the generation of the heterogeneous lithospheric mantle. *Chemical Geology* 628, 121471. https://doi.org/10.1016/j.chemgeo.2023.121471

Dai, W., Wang, Z., Liu, Y., Chen, C., Zong, K., Zhou, L., Zhang, G., Li, M., Moynier, F., Hu, Z. (2020) Calcium isotope compositions of mantle pyroxenites. *Geochimica et Cosmochimica Acta* 270, 144–159. https://doi.org/10.1016/j.gca.2019.11.024

Eriksen, Z.T., Jacobsen, S.B. (2022) Calcium isotope constraints on OIB and MORB petrogenesis: The importance of melt mixing. *Earth and Planetary Science Letters* 593, 117665. https://doi.org/10.1016/j.epsl.2022.117665

Eriksen, Z.T., Jacobsen, S.B., Day, J.M.D., White, W.M. (2024) Calcium isotope variability among ocean islands reveals the physical and lithological controls on mantle partial melting. *Geochimica et Cosmochimica Acta* 373, 326–341. https://doi.org/10.1016/j.gca.2024.02.011

Ganguly, J. (2010) Cation Diffusion Kinetics in Aluminosilicate Garnets and Geological Applications. *Reviews in Mineralogy and Geochemistry* 72, 559–601. https://doi.org/10.2138/rmg.2010.72.12

Hacker, B.R., Wallis, S.R., Ratschbacher, L., Grove, M., Gehrels, G. (2006) High-temperature geochronology constraints on the tectonic history and architecture of the ultrahigh-pressure Dabie-Sulu Orogen. *Tectonics* 25, TC5006. https://doi.org/10.1029/2005TC001937

He, D., Liu, Y., Moynier, F., Foley, S.F., Chen, C., Zhu, Y., Lü, X., Zhang, G., Zong, K. (2023) Tightly coupled Ca-Zn-Sr isotope co-variations in basalts caused by recycled calcium carbonate in the mantle source. *Chemical Geology* 637, 121678. https://doi.org/10.1016/j.chemgeo.2023.121678

Huang, S., Farkaš, J., Jacobsen, S.B. (2011) Stable calcium isotopic compositions of Hawaiian shield lavas: Evidence for recycling of ancient marine carbonates into the mantle. *Geochimica et Cosmochimica Acta* 75, 4987–4997. https://doi.org/10.1016/j.gca.2011.06.010

Huang, F., Zhou, C., Wang, W., Kang, J., Wu, Z. (2019) First-principles calculations of equilibrium Ca isotope fractionation: Implications for oldhamite formation and evolution of lunar magma ocean. *Earth and Planetary Science Letters* 510, 153–160. https://doi.org/10.1016/j.epsl.2018.12.034

Kang, J.-T., Zhu, H.-L., Liu, Y.-F., Liu, F., Wu, F., Hao, Y.-T., Zhi, X.-C., Zhang, Z.-F., Huang, F. (2016) Calcium isotopic composition of mantle xenoliths and minerals from Eastern China. *Geochimica et Cosmochimica Acta* 174, 335–344. https://doi.org/10.1016/j.gca.2015.11.039

Kang, J.-T., Ionov, D.A., Liu, F., Zhang, C.-L., Golovin, A.V, Qin, L.-P., Zhang, Z.-F., Huang, F. (2017) Calcium isotopic fractionation in mantle peridotites by melting and metasomatism and Ca isotope composition of the Bulk Silicate Earth. *Earth and Planetary Science Letters* 474, 128–137. https://doi.org/10.1016/j.epsl.2017.05.035

Li, J.-L., Wang, X.-S., Wang, Z., Huang, J., Gao, J. (2024) Ca–Zn isotope fractionation during fluid–rock interaction in subduction zones and its implication for deep carbon cycle. *Chemical Geology* 670, 122425. https://doi.org/10.1016/j.chemgeo.2024.122425

Li, Y., Wu, Z., Huang, S., Wang, W. (2022) Pressure and concentration effects on intermineral calcium isotope fractionation involving garnet. *Chemical Geology* 591, 120722. https://doi.org/10.1016/j.chemgeo.2022.120722

Li, Y., Hardin, J., Wang, W., Wu, Z., Huang, S. (2025) Mineral-melt calcium isotope fractionation factors constrained using *ab initio* molecular dynamics simulations and their implications to calcium isotope effects during partial melting in the upper mantle. *Geochimica et Cosmochimica Acta* 396, 51–70. https://doi.org/10.1016/j.gca.2025.02.032

Schauble, E.A. (2004) Applying Stable Isotope Fractionation Theory to New Systems. *Reviews in Mineralogy and Geochemistry* 55, 65–111. https://doi.org/10.2138/gsrmg.55.1.65

Smart, K.A., Tappe, S., Woodland, A.B., Greyling, D.R., Harris, C., Gussone, N. (2021) Constraints on Archean crust recycling and the origin of mantle redox variability from the $\delta^{44/40}$Ca – δ^{18}O – fO_2 signatures of cratonic eclogites. *Earth and Planetary Science Letters* 556, 116720. https://doi.org/10.1016/j.epsl.2020.116720

Tappe, S., Massuyeau, M., Smart, K.A., Woodland, A.B., Gussone, N., Milne, S., Stracke, A. (2021) Sheared Peridotite and Megacryst Formation Beneath the Kaapvaal Craton: a Snapshot of Tectonomagmatic Processes across the Lithosphere–Asthenosphere Transition. *Journal of Petrology* 62, egab046. https://doi.org/10.1093/petrology/egab046

Wang, Y., He, Y., Wu, H., Zhu, C., Huang, S., Huang, J. (2019) Calcium isotope fractionation during crustal melting and magma differentiation: Granitoid and mineral-pair perspectives. *Geochimica et Cosmochimica Acta* 259, 37–52. https://doi.org/10.1016/j.gca.2019.05.030

Xiao, Z.-C., Zhou, C., Kang, J.-T., Wu, Z.-Q., Huang, F. (2022) The factors controlling equilibrium inter-mineral Ca isotope fractionation: Insights from first-principles calculations. *Geochimica et Cosmochimica Acta* 333, 373–389. https://doi.org/10.1016/j.gca.2022.07.021

Zhu, H., Shan, Y., Liao, R., Zhang, L., Deng, J., Li, C., Du, L., Zhang, Z., Sun, W. (2025) Ca-Sr-Nd isotopic signatures of mid-ocean ridge basalts from the Central Indian Ridge and implications for recycled materials in the Indian Ocean mantle domain. *Chemical Geology* 673, 122546. https://doi.org/10.1016/j.chemgeo.2024.122546

Testing *ab initio* garnet-clinopyroxene Ca-isotope fractionation models with natural data

J. Munro, J.C. Lassiter, J.D. Barnes, A.M. Satkoski

Supplementary Information

The Supplementary Information includes:

1. Materials

Selected eclogites are from the Garnet Ridge serpentinized ultramafic breccia (SUM) diatreme, and have been well-studied to understand their origin (Helmstaedt and Doig, 1975; Smith *et al.*, 2004), trace their metamorphic history (Smith and Zientek, 1979; Usui *et al.*, 2006) and the evolution of the Colorado Plateau (Hoover *et al.*, 2020; Roden *et al.*, 1990; Smith *et al.*, 2004). They are widely regarded as fragments of subducted oceanic crust, possibly having originated from the Farallon slab (e.g., Helmstaedt and Doig, 1975). Similar mineralogical descriptions of eclogites from the neighbouring Moses Rock SUM diatreme (Usui *et al.*, 2006) suggest these xenoliths are representative for the region.

Mineralogical description

Mineral modal abundances (averaged point counting and least squares regression) are shown in Table S-1. Samples N350 and N371 have been the subject of several previous studies, including detailed petrologic descriptions, in Smith and Zientek (1979), Roden *et al.* (1990), and Smith *et al.* (2004). Most pyroxenes and garnets have triple junctions between each other, and many samples are mineralogically zoned, with garnet- or lawsonite-rich zones, potentially along a previous metamorphic fabric or line of fluid flow. Many samples are crosscut by fine fractures. Garnets frequently occur in samples as both small euhedral grains (<1 mm) within a weak fabric defined by the pyroxene, as well as larger, euhedral grains (>2 mm) with spongey cores and heavily fractured rims. Garnets contain inclusions of euhedral pyroxene, and lawsonite, and pyroxenes contain inclusions of garnet. Pyroxene frequently appears to be breaking down to lawsonite or zoisite. Pyroxene is typically <3 mm, with most larger grains clearly recrystallized along/near fractures. Rutile is present throughout all samples as a minor inclusion phase. Sample N350 contains minor, round, nodular pyrite grains up to 3mm across.

Table S-1 Lithology and mineral modal abundance for eclogitic xenoliths from Garnet Ridge, Navajo Volcanic Field.

Sample	Lithology	Mineralogy						
		cpx	grt	lawsonite	rutile	phengite	zoisite	pyrite
GR101	Eclogite	64	35	0	1			
GR105	Lawsonite eclogite	71	18	10	1			
GR110	Lawsonite eclogite	61	28	9	1	<1		
GR122	Eclogite	61	31	6	2			
GR130	Lawsonite-phengite eclogite	56	26	15	1	3		
GR182	Lawsonite eclogite	61	28	9	1	<1		
GR1j	Lawsonite eclogite	66	26	7	1			
N350-GR	Lawsonite-phengite eclogite	80	13	2.5	2	1.5		0.5
N371-GR	Eclogite	59	31	0	1	9	<1	<1

2. Analytical Methods

For grain mounts and stable isotope analysis, samples were crushed in a steel crusher, rinsed in dilute HCl and dried overnight in an oven. Optically clear and inclusion-free grain fragments of garnet and clinopyroxene were picked by hand. Because larger garnets often have spongey cores, this process likely preferentially sampled smaller garnet grains and inclusion-free rims of larger grains. Given the zoned nature of many larger garnet grains, this process also increases the likelihood that selected grains are in chemical and isotopic equilibrium with associated pyroxene grains.

Ca Isotope Ratios

Mineral separates were dissolved in HF + HNO_3 in an Anton-Paar Multiwave 7000 microwave. From the dissolved sample, a ~10 µg aliquot of Ca was mixed with ^{42}Ca-^{48}Ca double spike to correct for mass fractionation, and the mixture was dried down. The column chemistry to separate Ca followed the method of Huang *et al.* (2011), with the sample dissolved in 2.5M HCl and passed through a Teflon column packed with 250 µl of BioRad AG50W-X12 cation exchange resin. The sample solution was eluted in 1 ml of 2.5M HCl, and the eluate was run through the chemistry a second time to reduce contamination from K and Ti. The resulting solution was dried down. Samples were then analysed on a TE Triton TIMS, with Ca dissolved in 10% HNO3 and 10 µg of Ca was dried onto a single Re filament. Accuracy and precision of measurements were ensured by analysing the secondary standards IAPSO seawater (expected 1.88 ± 0.04‰, measured 1.92 ± 0.09‰, n=7), JP-1 (expected 1.14 ± 0.10‰, measured 1.22 ± 0.12‰, n=6) and BHVO-2 basalt (expected 0.80 ± 0.05‰, measured 0.91 ± 0.10‰, n=10). Expected values compiled from the geological standards reference database GeoRem (https://georem.mpch-mainz.gwdg.de/sample_query.asp). Repeat standard analyses yielded a single analysis precision of 0.13 ‰ or better (2σ) for $\delta^{44/40}Ca_{SRM915a}$ (Brooker *et al.*, 2024). The precision was improved by repeated analysis of samples, lowering the 2 standard error to 0.1‰ or less. https://georem.mpch-mainz.gwdg.de

Major elements

Major element compositions were determined on garnet and clinopyroxene in two sessions. In the first, epoxy-mounted, polished, carbon-coated pyroxene and garnet separates were analysed using the JEOL JXA-8200 electron microprobe in the Jackson School of Geosciences at the University of Texas at Austin. All analyses were made using a 10 nA beam current with a 15 keV accelerating voltage and a focused beam. Compositionally appropriate secondary standards were analysed periodically throughout each session to monitor analytical quality and instrumental drift (Pyrope NMNH 143968 for garnets and Diopside NMNH 117733 for clinopyroxenes). For both sessions peak count times were 20s and background 10s, and spots with anomalous totals were filtered out. Detections limits are typically ~0.1 wt.%. In the second session, a subset was analysed at Texas A&M University on a Cameca SXFive, using a 15 kV, 20 nA beam with a 3 µm spot size. This session was conducted mostly on polished, carbon-coated thin sections and was aimed at determining the heterogeneity of pyroxenes and garnet. In most samples the core and rim major element compositions are very similar, with flat Ca concentration profiles. The variation in GR105 pyroxene major element composition is significant, though, and the effect of this on temperature estimates is considered later. Spots were all chosen to avoid ablating inclusions.

Major element metadata available online through the Texas Data Repository: https://doi.org/10.18738/T8/P7XX0E.

3. Major Element Results

Table S-2 Major element data for garnet, clinopyroxene, lawsonite and zoisite from Garnet Ridge eclogites, Navajo Volcanic Field.

Sample	SiO_2	sd	TiO_2	sd	Al_2O_3	sd	Cr_2O_3	sd	FeO[a]	sd	MnO	sd	MgO	sd	CaO	sd	Na_2O	sd
Garnet																		
GR1j	37.38	0.28	0.22	0.13	20.79	0.43	-	-	29.21	0.94	1.77	1.09	3.12	0.4	8.15	0.84	0.01	0.02
GR101	37.24	0.64	0.09	0.08	21.64	0.31	-	-	28.35	1.22	1.015	1.01	4.49	1.91	6.32	1.78	0.03	0.04
GR105	38.52	0.7	0.13	0.11	21.4	0.51	0.02	0.02	27.89	1.34	1	0.53	5.78	2.01	5.96	2.09	0	0.02
GR110	37.96	0.51	0.06	0.05	20.92	0.46	0.02	0.02	29.09	0.64	1	0.72	3.98	0.9	7.15	1.25	0.02	0.02
GR122	37.1	0.43	0.2	0.14	20.97	0.52	-	-	29.51	0.75	1.55	0.89	3.03	1.3	7.55	1.2	0.05	0.02
GR130	37.99	0.52	0.06	0.07	21.18	0.62	0.05	0.03	29.34	0.51	1.19	0.71	4.27	1.3	6.5	1.74	0.02	0.03
GR182	37.66	0.46	0.07	0.07	20.97	0.34	0.02	0.02	31.47	1.18	0.85	0.42	3.36	0.49	6.01	0.75	0.01	0.02
N350	*37.53*	-	-	-	*21.22*		*0.05*	-	*30.93*		*1.11*	-	*4.19*	-	*5.98*	-	*0.01*	-
N371	37.82	0.29	0.1	0.08	21.44	0.73	-	-	29.3	2.07	0.37	0.29	5.75	1.49	5.34	0.07	0.02	0.02
Pyroxene																		
GR1j	55.61	0.43	0.05	0.03	9.29	1	0.01	0.04	7.94	0.68	0	0.01	7.14	0.39	11.57	0.58	7.43	0.34
GR101	56.38	0.35	0.07	0.04	10.56	1.01	0.03	0.02	5.04	1.17	0.04	0.04	8.1	0.95	11.61	1.39	7.67	0.71
GR105	57.29	0.7	0.07	0.03	15.59	3	0.03	0.02	5.18	1.86	0.04	0.04	4.39	1.06	6.51	1.84	10.46	1.15
GR110	55.93	0.34	0.05	0.03	9.19	0.72	0.02	0.02	5.76	0.44	0.05	0.04	8.74	0.42	12.93	0.67	6.86	0.36
GR122	55.46	0.26	0.07	0.06	11.45	0.94	0.02	0.01	7.23	0.61	0.04	0.01	5.28	0.28	8.6	0.71	9.23	0.29
GR130	56.64	0.41	0.06	0.03	12.89	1.52	0.05	0.02	4.81	1.82	0.01	0.01	6.85	0.91	10.43	1.1	8.29	0.57
GR182	56.57	0.37	0.04	0.03	12.78	1.61	0.04	0.03	4.96	0.28	0.02	0.01	6.52	0.94	10.32	1.52	8.39	0.85
N350	*57.83*	-	-	-	*16.16*	-	*0.03*	-	*3.86*		-	-	*4.94*	-	*6.78*	-	*11.19*	-
N371	56.3	0.54	0.07	0.04	10.99	1.22	0.02	0.03	5.13	1.64	0.04	0.04	7.72	1.1	11.27	1.86	7.8	1.01

[a] Total iron reported as FeO.
Analyses by electron microprobe. Major oxides reported in weight percent, and are averages of n samples.
Italicized data taken from personal communication D Smith.

Table S-2 continued.

Sample	K_2O	sd	NiO	sd	Total	Mg	Mineral composition	n	grains
Garnet									
GR1j	-	-	-	-	100.63	15	$Alm_{61}Grs_{23}Pyr_{12}Sps_4$	5	3
GR101	-	-	-	-	99.3	23	$Alm_{61}Pyr_{19}Grs_{18}Sps_2$	5	3
GR105	0.03	0.02	-	-	100.74	27	$Alm_{59}Pyr_{22}Grs_{17}Sps_2$	24	5
GR110	0.02	0.01	-	-	100.21	20	$Alm_{62}Grs_{20}Pyr_{16}Sps_2$	25	6
GR122	-	-	-	-	99.73	15	$Alm_{62}Grs_{22}Pyr_{12}Sps_4$	9	4
GR130	0.01	0.01	-	-	100.61	21	$Alm_{62}Grs_{18}Pyr_{17}Sps_3$	18	5
GR182	0.01	0.01	-	-	100.42	16	$Alm_{68}Grs_{17}Pyr_{13}Sps_2$	19	5
N350	*0.01*	-	-	-	*101*	19	$Alm_{64}Grs_{17}Pyr_{17}Sps_2$	-	-
N371	-	-	-	-	100.14	19	$Alm_{60}Grs_{19}Pyr_{16}Sps_4$	3	3
Pyroxene									
GR1j	0	0.01	-	-	99.04	73	$Jd_{43}Di_{46}Ac_{11}$	22	6
GR101	0	0.01	0.03	0.03	99.51	85	$Jd_{47}Di_{46}Ac_7$	25	7
GR105	0	0.01	0.03	0.04	99.55	67	$Jd_{70}Di_{26}Ac_4$	29	9
GR110	0.01	0.01	0.02	0.02	99.53	84	$Di_{51}Jd_{40}Ac_9$	24	7
GR122	-	0	0	0.01	97.39	75	$Jd_{53}Di_{34}Ac_{13}$	4	2
GR130	0	0.01	0.04	0.04	99.56	77	$Jd_{56}Di_{41}Ac_3$	24	7
GR182	0	0.01	0.02	0.03	99.67	75	$Jd_{56}Di_{40}Ac_3$	32	9
N350	*0.02*	-	-	-	*100.82*	*70*	*$Jd_{75}Di_{25}Ac_0$*	-	-
N371	0	0.01	0.03	0.03	99.33	82	$Jd_{49}Di_{44}Ac_7$	24	7

[a] Total iron reported as FeO.
Analyses by electron microprobe. Major oxides reported in weight percent, and are averages of n samples.
Italicized data taken from personal communication D Smith.

4. $\delta^{44/40}$Ca Data

$\delta^{44/40}$Ca values for NVF are summarized in Table S-3, and literature sample $\delta^{44/40}$Ca values, CaO wt.% and modal abundances for pyroxenes and garnet are presented in Table S-4.

Table S-3 Garnet Ridge eclogite sample stable calcium isotope data.

Sample	Lithology	$\delta^{44/40}$Ca vs SRM915a (‰) ± 2SE		
		garnet (n=2)	omphacite (n=2)	$\Delta^{44/40}Ca_{grt\text{-}cpx}$ [1]
GR101	Eclogite	1.68 ± 0.04	0.76 ± 0.02	0.92 ± 0.10
GR105	Lawsonite eclogite	1.70 ± 0.09	0.85 ± 0.01	0.85 ± 0.10
GR110	Lawsonite eclogite	1.80 ± 0.07	0.69 ± 0.04	1.11 ± 0.10
GR122	Eclogite	1.75 ± 0.04	1.35 ± 0.10	0.40 ± 0.10
GR130	Lawsonite-phengite eclogite	1.98 ± 0.04	1.11 ± 0.09	0.87 ± 0.11
GR182	Lawsonite eclogite	1.97 ± 0.08	1.21 ± 0.04	0.76 ± 0.10
GR1j	Lawsonite eclogite	1.77 ± 0.04	1.06 ± 0.08	0.71 ± 0.10
N350-GR	Lawsonite-phengite eclogite	1.68 ± 0.02	0.96 ± 0.01	0.72 ± 0.10
N371-GR	Eclogite	1.54 ± 0.04	0.90 ± 0.04	0.64 ± 0.10

[1] 2SE of long-term standards IAPSO and BHVO-2 used (0.10‰ per analysis, 0.14‰ propagated error, see Section 8).

The range of $\delta^{44/40}$Ca values for clinopyroxene and garnet in mantle eclogites are shown in Figure S-1, together with literature values for: xenolithic eclogites from Roberts Victor (Chen *et al.*, 2020), Bellsbank (Smart *et al.*, 2021) and Udachnaya Kimberlites (Kang *et al.*, 2019); Dabie eclogites and Sulu garnet lherzolites from the Dabie-Sulu Orogen, North China (Wang *et al.*, 2019); xenolith garnet lherzolites from Slave Craton (Brooker *et al.*, 2024); sheared garnet peridotites from Premier Kimberlite, South Africa (Tappe *et al.*, 2021); and garnet pyroxenites from Hannouba Basaltic Plateau (Dai *et al.*, 2020). Overall, the clinopyroxene $\delta^{44/40}$Ca values of NVF eclogites overlap and extend to slightly higher values than previous work, whereas the garnet $\delta^{44/40}$Ca values are all significantly higher than most previous data (Fig. S-1).

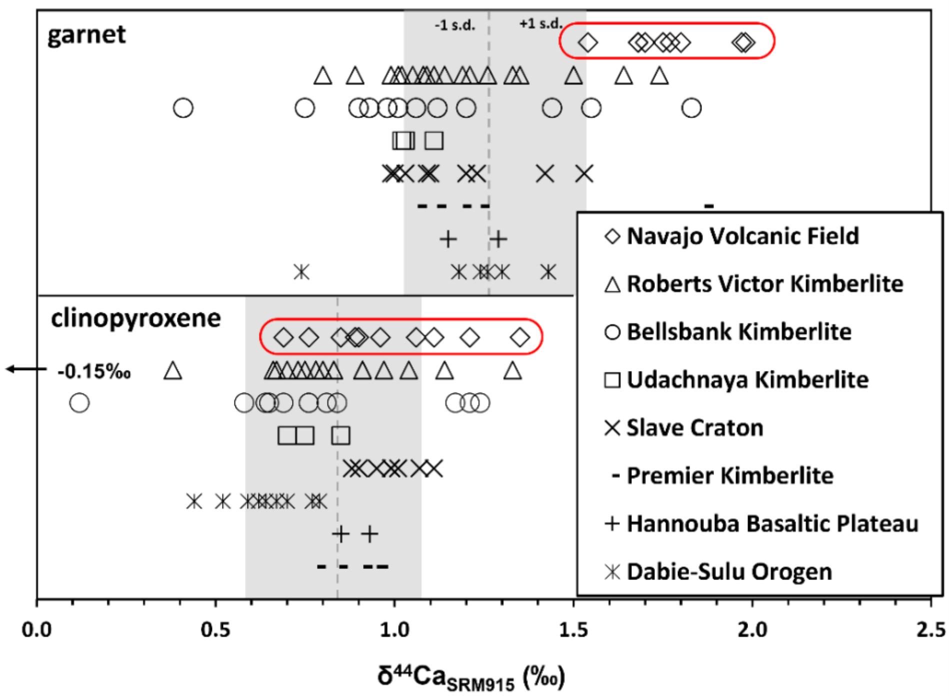

Figure S-1 Compilation of garnet and clinopyroxene calcium isotope composition ($\delta^{44/40}$Ca) of samples in this study (diamonds) compared to literature data for eclogites, garnet peridotites and pyroxenites (see text for references). The dashed lines and grey fields in represent the average and 1σ, respectively.

Data for literature samples are included in Table S-4, where garnet and pyroxene modal abundances, CaO wt.% and $\delta^{44/40}$Ca values are summarized.

Table S-4 Literature Ca isotope data, and garnet-pyroxene modal abundances and CaO contents.

Sample	Lithology	Modal abundance		CaO wt.%		$\delta^{44/40}$Ca vs SRM915a (‰)			
		garnet	pyroxene	garnet	pyroxene	garnet	pyroxene	$\Delta^{44/40}Ca_{grt-cpx}$	2SE*
Roberts Victor Kimberlite, South Africa (Chen *et al.*, 2020)									
Type I									
RV07-02	Eclogite	28	73	14.36	4.25	1.19	0.83	0.36	0.08
RV07-03	Eclogite	62	38	14.84	5.20	1.09	0.91	0.18	0.12
RV07-09a	Eclogite	25	53	14.45	3.59	1.08	0.75	0.33	0.08
RV07-13	Eclogite	42	58	13.40	4.18	1.26	0.97	0.29	0.09
RV07-20	Eclogite	55	45	17.40	4.46	1.33	0.8	0.53	0.13
RVF-8	Eclogite	50	50	13.83	5.35	0.89	0.67	0.22	0.08
RV07-01	Eclogite	42	58	14.11	4.72	1.11	0.78	0.33	0.08
RV07-07	Eclogite	55	45	13.98	4.68	1.26	0.91	0.35	0.10
RV07-11	Eclogite	53	47	14.39	4.53	1.35	0.83	0.52	0.08
RV07-14	Eclogite	70	30	13.88	4.81	1.21	0.66	0.55	0.08
Type II									
RV07-12	Eclogite	48	52	18.04	6.79	1.5	0.7	0.8	0.12
RV73-12	Eclogite	45	55	18.63	4.26	0.8	-0.15	0.95	0.13
RV07-08	Eclogite	40	60	14.46	11.28	1.14	1.04	0.1	0.08
RV07-30	Eclogite	50	50	14.66	7.58	1.05	0.78	0.27	0.08
RV07-31	Eclogite	50	50	15.46	9.51	0.99	1.14	-0.15	0.08
RV07-33	Eclogite	50	50	15.05	10.35	1.01	0.91	0.1	0.12
RV07-34	Eclogite	50	50	14.33	13.58	1.02	1.33	-0.31	0.10
Bellsbank Kimberlite, South Africa (Smart *et al.*, 2021)									
DGE-1	Eclogite	55	45	16.63	3.86	0.9	0.76	0.14	0.13
DGE-2	Eclogite	55	45	16.41	12.16	1.01	0.76	0.25	0.07
DGE-3	Eclogite	55	45	16.69	3.86	0.93	0.58	0.35	0.10
DGE-4	Eclogite	55	45	17.12	10.47	1.55	1.21	0.34	0.10
DGE-8	Eclogite	55	45	15.98	10.67	1.2	0.84	0.36	0.10
DGO-5	Eclogite	55	45	15.62	10.81	1.12	0.81	0.31	0.10
DGO-6	Eclogite	55	45	15.26	9.01	0.98	0.69	0.29	0.10
DGO-7	Eclogite	55	45	16.95	11.10	1.83	1.24	0.59	0.07
DGO-8	Eclogite	55	45	17.44	5.07	0.41	0.12	0.29	0.10
DGO-11	Eclogite	55	45	15.08	11.17	1.06	0.64	0.42	0.10
DGO-14	Eclogite	55	45	13.41	11.22	1.44	1.17	0.27	0.10
DGO-15	Eclogite	55	45	11.48	15.28	0.75	0.65	0.1	0.10
Udachnaya Kimberlite, Russia (Kang *et al.*, 2019)									
U-400	Eclogite	55	45	14.20	7.52	1.03	0.85	0.18	0.11
U-401	Eclogite	55	45	20.56	12.75	1.02	0.7	0.32	0.11
U-402	Eclogite	55	45	16.88	4.72	1.11	0.75	0.36	0.11
Slave Craton, Canada (Brooker *et al.* 2024 & references therein)									
MX 158	Garnet lherzolite	10	5	19.543	5.09	1.42	0.90	0.52	0.14
MX5001	Garnet lherzolite	10	5	19.664	5.35	1.00	0.88	0.12	0.13
DDM-149	Garnet lherzolite	25	4	18.00	4.21	1.23	1.07	0.16	0.14
DDM-327	Garnet lherzolite	20	4	17.80	4.80	0.99	0.99	0.00	0.10
DDM-335	Garnet lherzolite	20	5	17.90	5.80	1.10	1.01	0.09	0.14
DDM-359	Garnet lherzolite	10	5	-	-	1.20	1.11	0.09	0.14
DDM-360	Garnet lherzolite	20	5	18.90	4.60	1.03	0.95	0.08	0.14
DDM-361	Garnet lherzolite	15	5	18.69	6.86	1.53	1.11	0.42	0.14
DDM-368	Garnet lherzolite	10	5	19.10	5.82	1.09	0.99	0.10	0.12

*2σ of $\Delta^{44/40}Ca_{grt-cpx}$ using the standard deviation of internal standard used for study (e.g. BHVO-2, IAPSO, etc.), and propagating error using Eq. S-9 in Section 8.

Table S-4 continued.

Sample	Lithology	Modal abundance		CaO wt.%		$\delta^{44/40}$Ca vs SRM915a (‰)			
		garnet	pyroxene	garnet	pyroxene	garnet	pyroxene	$\Delta^{44/40}Ca_{grt-cpx}$	2SE*
Premier Kimberlite, South Africa (Tappe *et al.*, 2021)									
CIM 15-003	Garnet peridotite	7	6	4.88	16.42	1.24	0.91	0.33	0.07
CIM 15-021	Garnet peridotite	7	4	4.75	16.18	1.06	0.96	0.11	0.07
CIM 15-022	Garnet peridotite	12	7	4.56	16.015	1.12	0.78	0.34	0.07
CIM 15-035	Garnet peridotite	15	5	6.085	18.775	1.19	0.84	0.35	0.07
CIM 15-040	Garnet peridotite	11	5	4.74	20.04	1.87	0.95	0.92	0.07
Hannouba Basaltic Plateau, China (Dai *et al.*, 2020)									
DMP441-PY	Garnet pyroxenite	39	41	19.6	4.21	1.15	0.93	0.22	0.11
DMP464-PV	Garnet pyroxenite	54	40	19.9	4.47	1.29	0.85	0.44	0.11
Dabie-Sulu Orogen, China (Wang *et al.*, 2019)									
BXL-1	Eclogite	54	33	14.43	7.73	0.74	0.59	0.15	0.03
BXL-4	Eclogite	52	34	14.05	8.27	1.26	0.64	0.62	0.03
BXL-6	Eclogite	60	30	13.58	8.21	1.43	0.62	0.81	0.04
HA-3	Eclogite	-	-	12.5	9.36	1.3	0.52	0.78	0.04
HA-4	Eclogite	-	-	12.92	10.5	1.24	0.44	0.8	0.04
SH-1	Eclogite	-	-	13.52	9.23	1.18	0.67	0.51	0.04
SH-5	Eclogite	-	-	14.31	8.4	1.18	0.7	0.48	0.04
ZMF-2	Garnet lherzolite	-	-	21.44	4.6	1.43	0.77	0.66	0.04
ZMF-3	Garnet lherzolite	-	-	22.46	4.65	1.43	0.79	0.64	0.05

*2σ of $\Delta^{44/40}Ca_{grt-cpx}$ using the standard deviation of internal standard used for study (e.g. BHVO-2, IAPSO, etc.), and propagating error using Eq. S-9 in Section 8.

5. Estimation of Sample Equilibration Temperatures

Estimating temperatures

Because temperature estimates are important to compare natural data to the first principles models, the error and scatter produced by different methods for processing data must be mitigated. Across the limited dataset of Bellsbank, Roberts Victor, Premier, Hannouba and Dabie-Sulu samples there are two different garnet-pyroxene Fe^{2+}-Mg^{2+} thermometers commonly used in previous studies, and three different Fe^{3+} corrections applied, whereas the Slave Craton temperatures reported in the literature are based on the Köhler and Brey (1990) clinopyroxene-orthopyroxene thermometer, which is not necessarily consistent with the garnet-clinopyroxene thermometer. To remove potential systematic biases in temperature estimates between different studies, all temperatures were recalculated using the same procedure outlined below. All Fe^{3+} corrections on clinopyroxene and garnet followed Droop (1987), and five thermometers were applied: those of Ellis and Green (1979), Krogh (1988), Powell (1985), Ravna (2000), and Sudholz *et al.* (2022). These thermometers are all based on the Fe^{2+}-Mg^{2+} exchange between garnet and clinopyroxene, and subsequent ones build on previous work, with modified calibrations. These five thermometers were averaged to get a final temperature estimate.

In Figure S-2, it can be seen that the method applied in this reliably reproduces much of the literature temperature estimates within error (typically ≤50 °C; Krogh Ravna and Paquin, 2003). The standard deviation of temperature estimates from the five thermometers varied between 18 and 129 °C (average 1σ = 53 °C). Erring on the side of caution, the temperature error allocated to each sample is the standard deviation from the averaging of thermometers or 50 °C, whichever is highest. The 50 °C threshold is because this is a typically reported error for Mg-Fe exchange thermometry (Krogh Ravna and Paquin, 2003).

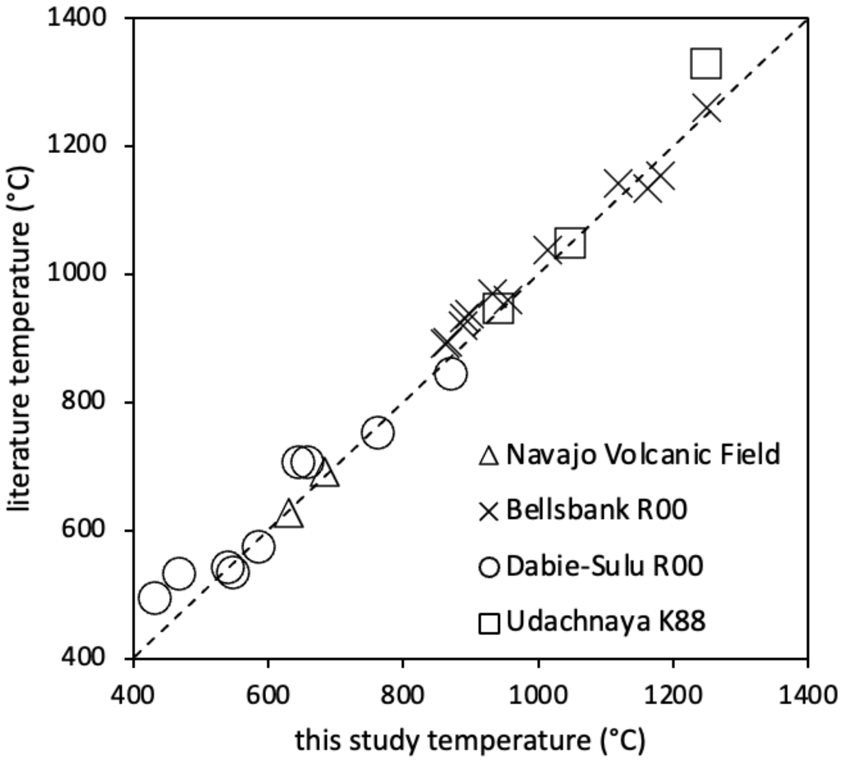

Figure S-2 Comparison of temperature estimates from literature and this study for eclogites from Dabie-Sulu (using Ravna, 2000), Bellsbank kimberlite (Ravna, 2000) Udachnaya (Krogh, 1988), and Navajo Volcanic Field (pseudosection work, Smith *et al.*, 2004).

Temperatures used for all samples are summarized in Table S-5 and literature temperatures are shown for reference. For NVF samples, temperatures were most consistent with published temperatures for GR1 and N350 (Smith *et al.*, 2004) when the pressure is set to 3.6 GPa.

Table S-5 Compilation of pressure and temperature estimates for samples from this study and literature. Literature pressure estimates are in the first column. The five Fe-Mg garnet-pyroxene thermometers used in this study are shown, and are averaged to yield the estimated temperature used in this study. Literature estimates of temperature are shown for comparison. Standard deviation is calculated from the five thermometers used to find an average temperature.

	P (GPa)	Temperature estimates in this study (°C)								Literature
Sample	Lit	REE	Ellis&Green79	Powell85	Krogh88	Ravna00	Sudholz22	Average	1SD	T (°C)
Navajo Volcanic Field (this study)										
GR101	3.6		550	523	477	514	564	526	30	
GR105	3.6		828	805	766	840	941	836	58	
GR110	3.6		547	520	482	507	543	520	34	
GR122	3.6		610	584	553	585	617	590	23	
GR130	3.6		625	599	557	600	656	607	33	
GR182	3.6		584	557	509	545	624	564	39	
GR1j	3.6		638	613	585	617	636	618	19	
N350-GR	3.6		697	671	627	683	774	691	48	684
N371-GR	3.6		569	542	502	548	577	548	26	
GR1	3.6		644	617	569	621	683	627	37	630

Table S-5 continued.

Sample	P (GPa) Lit	Temperature estimates in this study (°C) REE	Ellis&Green79	Powell85	Krogh88	Ravna00	Sudholz22	Average	1SD	Literature T (°C)
Bellsbank Kimberlite (Smart *et al.*, 2021)										
DGE-1	4.3	854	1153	1140	1076	1174	1234	1155	51	1182
DGE-2	5.9	877	1252	1244	1293	1351	1164	1261	61	1249
DGE-3	4.2	818	1136	1122	1056	1150	1213	1135	50	1163
DGE-4	2.9	953	948	933	940	911	869	920	28	889
DGE-8	2.9	964	919	903	906	889	848	893	24	862
DGO-5	3	1014	971	957	967	927	871	939	37	899
DGO-6	2	1042	927	912	909	851	872	894	28	865
DGO-7	4	855	1059	1046	1067	1060	960	1038	40	1015
DGO-8	2	859	986	971	919	907	1022	961	43	956
DGO-11	3.2	876	1003	990	1004	964	895	971	41	933
DGO-14	2.8	711	967	953	963	914	862	932	40	891
DGO-15	5.3	605	1170	1162	1170	1210	1003	1143	72	1118
Roberts Victor Kimberlite (Huang *et al.*, 2012)										
Type I										
HRV77bimin	6		1261	1250	1225	1403	1437	1315	87	1191
HRV77megaC	6		1165	1150	1167	1266	1213	1192	43	1126
RV07-02	4.5	829	993	972	906	993	1067	986	52	1060
RV07-03	5.7	991	1119	1101	1073	1200	1217	1142	57	1205
RV07-09a	4.8	765	1056	1036	959	1099	1166	1063	68	1110
RV07-09b	6		1067	1045	969	1159	1211	1090	86	1099
RV07-13	4.4	851	1008	987	922	1037	1106	1012	60	1040
RV07-20	4.5	874	993	972	911	999	1046	984	44	1060
RV07-41	6		1226	1212	1136	1336	1412	1264	98	1075
RVF-5	6		1004	980	914	1029	1062	998	50	1112
RVF-6	6		922	896	851	972	972	923	46	1060
RVF-7	6		1196	1181	1154	1348	1383	1252	94	1125
RVF-8	4.5	961	992	971	933	998	1039	987	35	1050
RV07-01	4.5	836	1144	1130	1090	1181	1231	1155	48	1060
RV07-07	4.6	871	1004	984	929	1004	1059	996	42	1075
RV07-11	4.4	874	1118	1103	1055	1147	1207	1126	50	1055
RV07-14	4.5	907	1013	992	941	1009	1062	1003	39	1070
RV07-16	6	1152	1170	1156	1184	1251	1171	1187	33	1170
RV07-18	5.9	807	1227	1214	1190	1331	1349	1262	65	1138
RV07-19	6	1078	1194	1180	1189	1291	1256	1222	44	1162
RV07-22	5.9		1192	1176	1139	1283	1316	1221	67	1131
RV07-29a	6		1188	1173	1159	1282	1274	1215	52	1141
RV07-29b	6		1089	1069	1045	1147	1138	1098	39	1139
RV06 BG-1	6		1253	1245	1296	1369	1224	1277	51	1267
RV07-05a	6		1311	1309	1267	1380	1091	1272	97	1232
RV07-05b	6		1253	1244	1295	1355	1212	1272	49	1245
RV07-23a	6		1197	1184	1219	1300	1213	1222	41	1189
RV07-23b	6		1187	1173	1177	1286	1260	1217	47	1140
RV07-25	6		1014	993	994	1064	1005	1014	26	1192
Type II										
RV07-12	3.5	1007	914	894	870	902	935	903	22	915
RV07-36	5.7		1030	1007	947	1075	1127	1037	61	1066
RV07-66	4.5		1002	982	945	969	975	974	18	897
RV73-12	3.5	909	852	827	753	791	883	821	46	995
RV07-39	6		976	950	865	1022	1101	983	78	1013
BD1186	6		1239	1229	1278	1370	1246	1273	52	1220
BD1191	6		1220	1209	1252	1355	1267	1261	52	1194
RV07-08	5.1	884	1150	1139	1173	1236	1130	1166	38	1150
RV07-30	6.6	1127	1161	1144	1162	1271	1228	1193	48	1290
RV07-31	5.5	1068	1113	1099	1125	1181	1104	1125	30	1190
RV07-33	6.6	1104	1177	1163	1200	1290	1177	1202	46	1290

RV07-34	6.9	879	1325	1319	1366	1493	1303	1361	69	1320
RV07-37	6.1	1146	1163	1148	1160	1276	1247	1199	52	1188

Table S-5 continued.

	P (GPa)	Temperature estimates in this study (°C)								Literature T (°C)
Sample	Lit	REE	Ellis&Green79	Powell85	Krogh88	Ravna00	Sudholz22	Average	1SD	
Udachnaya Kimberlite (Kang *et al.*, 2019)										
U-400	5		1033	1015	1017	1098	1092	1051	36	1047
U-401	5		977	961	965	992	843	948	53	940
U-402	5		1314	1309	1294	1394	1347	1331	36	1247
Slave Craton (Brooker *et al.* 2024 & references therein)										
MX 158	6.8		969	943	897	973	917	940	29	1200
MX5001	6.2		1146	1128	1105	1182	1102	1132	30	1261
DDM_149	5.7	942	1234	1221	1178	1289	1240	1232	36	1255
DDM_327	6.6	1132	1366	1359	1352	1505	1393	1395	57	1288
DDM_335	6.3		1273	1262	1265	1358	1237	1279	41	1332
DDM_360	5.8	955	1315	1307	1287	1405	1320	1327	41	1257
DDM_361	8	1653	1280	1265	1290	1411	1236	1297	60	1305
DDM_367	6.3	1378	1048	1027	1014	1065	765	984	111	1285
DDM_368	5.9	1214	1227	1214	1210	1286	919	1171	129	1247
Premier Kimberlite (Tappe *et al.*, 2021)										
CIM 15-003	5.2	1170	1171	1156	1124	1184	1127	1152	24	1299
CIM 15-021	5.5	1170	1215	1202	1171	1252	1190	1206	27	1302
CIM 15-022	5.3	1107	1235	1224	1190	1276	1222	1229	28	1303
CIM 15-035	4.8	1186	999	979	951	960	928	963	24	1088
CIM 15-040	2.8	866	910	889	823	795	856	854	42	809
Hannouba Basaltic Plateau, China (Dai *et al.*, 2020)										
DMP441-PY	1.51		1117	1111	1054	1000	1084	1073	43	1004
DMP464-PV	1.26		1420	1440	1435	1394	1358	1409	30	1025
Dabie-Sulu Orogen (Wang *et al.*, 2019)										
BXL-1	3		625	600	565	549	529	573	34	586
BXL-4	3		575	550	519	518	502	533	26	549
BXL-6	3		583	558	528	527	513	542	25	541
HA-3	1.7		574	552	526	481	524	531	31	468
HA-4	1.7		540	518	492	445	468	493	34	432
SH-1	2.8		743	721	705	698	657	705	28	658
SH-5	2.8		739	717	697	697	675	705	21	645
ZMF-2	4.9		908	883	821	871	738	844	60	872
ZMF-3	4.9		820	793	727	763	658	752	56	764

It is assumed that all NVF eclogites formed at roughly the same depth and this value is consistent with suggested literature pressures of ~3.3 GPa (Smith *et al.*, 2004). Therefore, 3.6 GPa is used for all. For most samples, our temperature estimates and the literature values are within error. An exception is the Roberts Victor eclogites, as it appears that no Fe^{2+}-Fe^{3+} correction was made in determining the literature temperature (Gréau *et al.*, 2011). 'Average' temperatures in Table S-5 were used in plotting Figure 1.

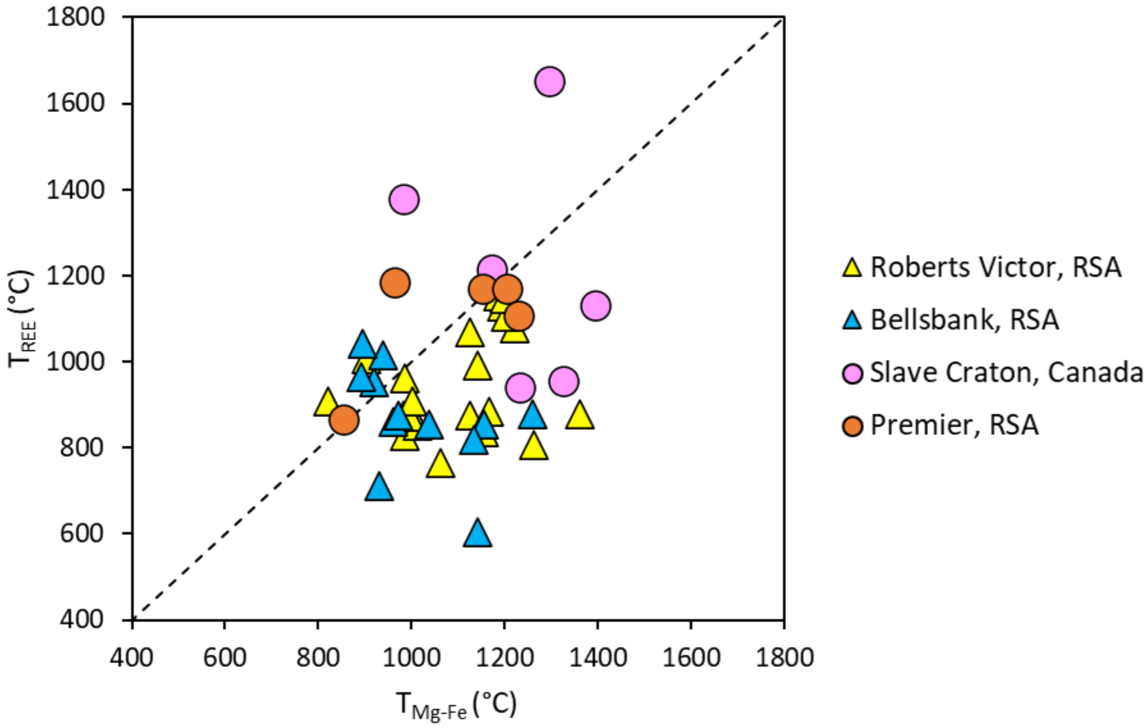

Figure S-3 Comparison of temperature estimates from Mg-Fe exchange thermometry and rare earth element in garnet and clinopyroxene thermobarometry of Sun and Liang (2015). Note that here, Mg-Fe thermometry typically yields higher temperature estimates.

The T_{REE} estimates are based on published literature data. Details such as where the REEs were measured (rims, cores, whole-grain averages), whether grains were zoned, number of duplicates, and whether garnet and clinopyroxene were in equilibrium are unknown, and therefore scatter in calculated T_{REE} estimates may reflect these uncertainties. Any apparent trends should be interpreted with caution, beyond noting that $T_{Mg\text{-}Fe}$ and T_{REE} values are often not aligned on a 1:1 line.

Temperature zonation in NVF eclogites

Because the grains in the NVF eclogites are zoned, it is important to ensure that the calculated temperatures are representative. Four samples were analysed for their mineral grain core and rim major element compositions. For each, three garnet and three clinopyroxene grains were measured and it was assumed that the rims/cores of the garnet were in equilibrium with the rims/cores of the clinopyroxene. The estimated temperatures are shown in Table S-6. The rims all record higher temperatures, showing that the growth of garnet and jadeite was on a prograde path. Although some of these temperature variations are large, it can be seen from Figure S-4 that the core and rim temperature estimates are mostly within the standard error expected from the thermometry (generally 50 °C), and that the zonation does not shift the predicted bulk temperature significantly. Hence, as the Ca isotope values are determined on bulk garnet and jadeite grains, the 'bulk temperature' is calculated from the average garnet and clinopyroxene major element content. For GR105, the core-rim temperature variation is large and the sample has clearly been heated significantly prior to emplacement. For this sample the average is still used, to keep the method consistent with temperature estimates from literature.

Table S-6 Summary of temperature estimates for core and rims of zones garnet-clinopyroxene pairs in NVF eclogites.

	Temperature (°C)			
sample	**bulk**	**core**	**rim**	**rim - core**
GR105	836	759	895	137
GR110	531	529	543	13
GR130	607	588	633	45
GR182	564	550	603	53

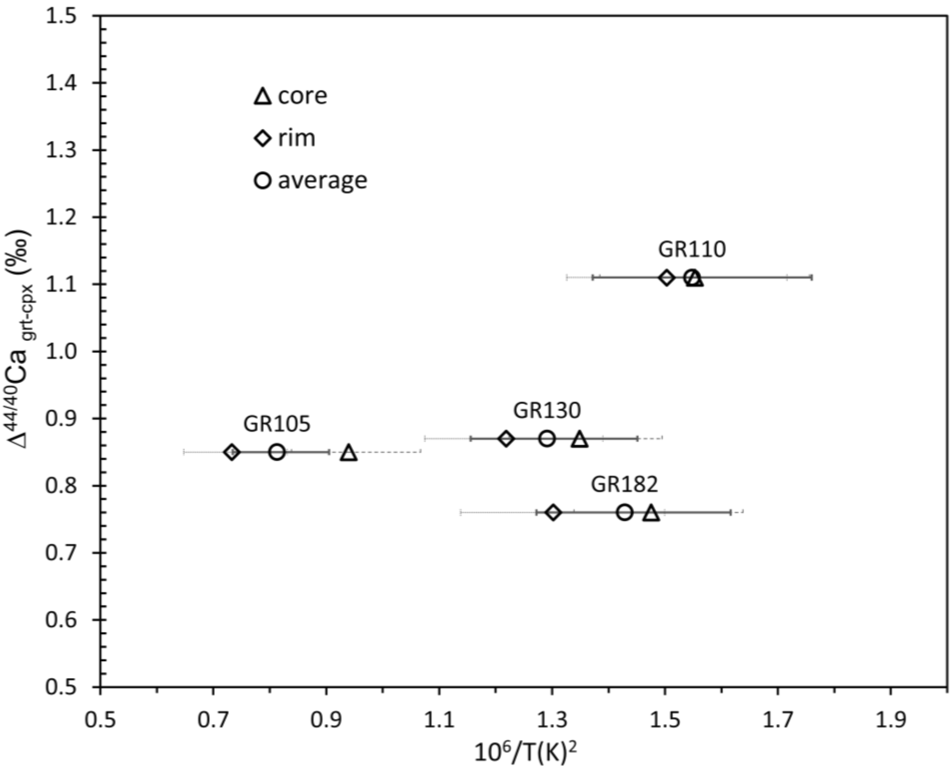

Figure S-4 Comparison of temperature estimates for Navajo Volcanic Field eclogites using: averaged garnet and clinopyroxene major element data to get average, whole-grain temperatures (circles), core-core garnet-clinopyroxene temperature estimates (triangles) and rim-rim temperature estimates (diamonds). Bold error bars are 1 standard error for the average grain temperature estimate, assuming a temperature estimate error of ±50 °C.

6. Analysis of Fractionation Model and Residuals

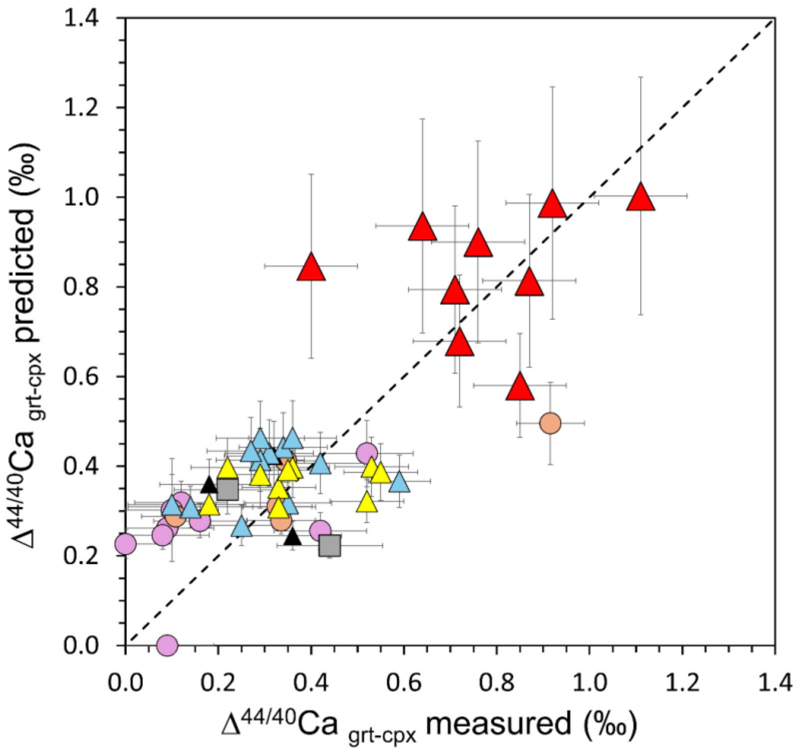

Figure S-5 $\Delta^{44/40}Ca_{grt\text{-}cpx}$ measured for natural samples versus the predicted $\Delta^{44/40}Ca_{grt\text{-}cpx}$ determined from Eq. 2. Error bars equivalent to 2SE, and symbols as for Figure 1.

Constraining the controls on natural $\Delta^{44/40}Ca_{grt\text{-}cpx}$ variability

To test the effect of garnet composition, garnet almandine, pyrope, and grossular proportions, and garnet CaO and Al_2O_3 wt.% were plotted against temperature-corrected residuals. To remove temperature effects, the measured $\Delta^{44/40}Ca_{grt\text{-}cpx}$ is divided by $10^6/T^2$. Then, the model value (Eq. 1) calculated at $10^6/T^2 = 1$ is subtracted from this adjusted $\Delta^{44/40}Ca_{grt\text{-}cpx}$ – this is the temperature-corrected residual. The temperature-corrected residual parameters used in Figure 2 are summarized in Table S-7. The dashed lines in Figure 2 represent the maximum expected compositional effects at 1000 K, assuming linear mixing. Expected compositional variation is typically less than the error on the residuals. Pressure variation based on Li *et al.* (2022) prediction of <0.05 ‰ at 1000 K from 1-10 GPa.

No statistically-significant correlations were seen, with the 'best' correlation being residual versus grossular content (p-value = 0.08, Fig. 2a). To test the effect of clinopyroxene composition, diopside content and CaO wt.% were plotted versus residuals. The lack of correlation is evident in Figure 2b where residual versus diopside content (p-value = 0.09) is shown. No jadeite effect is seen when jadeite content of pyroxenes is compared to residuals (p-value = 0.12, Fig. 2c). Pressure effects cannot be properly tested, since no accurate, independent geobarometer could be applied to all samples. However, where literature pressure estimates are plotted versus residuals (p-value = 0.31, Fig. 2d), no correlation is seen.

Table S-7 Data used for Figure 2, with measured $\Delta^{44/40}Ca_{grt-cpx}$ and $10^6/T^2$ used to calculate temperature-corrected residuals, measured $\Delta^{44/40}Ca_{grt-cpx}/10^6/T^2$ and temperature-corrected residuals. Almandine, grossular, pyrope, jadeite and diopside contents, and literature pressure estimates are included and plotted against residuals in Figure 2.

Sample	measured $\Delta^{44/40}Ca_{grt-cpx}$	$10^6/T^2$	measured $\Delta^{44/40}Ca_{grt-cpx}$ / 106/T2	Residual: (measured $\Delta^{44/40}Ca_{grt-cpx}$ / $10^6/T^2$) - (predicted $\Delta^{44/40}Ca_{grt-cpx}$ at $10^6/T^2$ =1)	almandine content	grossular content	pyrope content	jadeite content	diopside content	literature pressure estimate (GPa)
Navajo Volcanic Field, USA (this study)										
GR101	0.92	1.57	0.59	-0.04	61	18	19	47	46	3.6
GR105	0.85	0.92	0.92	0.29	59	17	22	70	26	3.6
GR110	1.11	1.59	0.70	0.07	62	20	16	40	51	3.6
GR122	0.4	1.34	0.30	-0.33	62	22	12	53	34	3.6
GR130	0.87	1.29	0.67	0.04	62	18	17	56	41	3.6
GR182	0.76	1.43	0.53	-0.10	68	17	13	56	40	3.6
GR1j	0.71	1.26	0.56	-0.07	61	23	12	43	46	3.6
N350-GR	0.72	1.08	0.67	0.04	64	17	17	75	25	3.6
N371-GR	0.64	1.49	0.43	-0.20	60	19	16	49	44	3.6
Roberts Victor Kimberlite (Huang *et al.*, 2012)										
RV07-02	0.36	0.63	0.57	-0.06	34	11	54	32	63	4.5
RV07-03	0.18	0.50	0.36	-0.27	35	14	50	28	65	5.7
RV07-09a	0.33	0.56	0.59	-0.04	34	9	55	26	67	4.8
RV07-13	0.29	0.61	0.48	-0.15	37	11	50	32	61	4.4
RV07-20	0.53	0.63	0.84	0.21	33	12	54	13	79	4.5
RVF-8	0.22	0.63	0.35	-0.28	34	14	51	35	59	4.5
RV07-01	0.33	0.49	0.67	0.04	29	12	57	40	60	4.5
RV07-07	0.35	0.62	0.56	-0.07	31	12	56	36	59	4.6
RV07-11	0.52	0.51	1.02	0.39	31	12	57	37	63	4.4
RV07-14	0.55	0.61	0.90	0.27	29	12	57	38	58	4.5
RV07-12	0.8	0.72	1.11	0.48	42	18	39	23	74	3.5
RV73-12	0.95	0.84	1.14	0.51	33	11	54	18	78	3.5
RV07-08	0.1	0.48	0.21	-0.42	39	30	30	42	58	5.1
RV07-30	0.27	0.47	0.58	-0.05	36	26	43	36	60	6.6
RV07-31	-0.15	0.51	-0.29	-0.92	36	26	38	35	62	5.5
RV07-33	0.1	0.46	0.22	-0.41	37	28	35	35	58	6.9
RV07-34	-0.31	0.37	-0.83	-1.46	35	37	28	42	58	6.9

Table S-7 continued.

Sample	measured $\Delta^{44/40}Ca_{grt-cpx}$	$10^6/T^2$	measured $\Delta^{44/40}Ca_{grt-cpx}$ / 106/T2	Residual: (measured $\Delta^{44/40}Ca_{grt-cpx}$ / $10^6/T^2$) - (predicted $\Delta^{44/40}Ca_{grt-cpx}$ at $10^6/T^2=1$)	almandine content	grossular content	pyrope content	jadeite content	diopside content	literature pressure estimate (GPa)
Bellsbank Kimberlite (Smart *et al.*, 2021)										
DGE-1	0.14	0.49	0.29	-0.34	27	10	63	28	72	4.3
DGE-2	0.25	0.43	0.59	-0.04	24	32	43	36	64	5.9
DGE-3	0.35	0.50	0.69	0.06	27	10	62	28	72	4.2
DGE-4	0.34	0.70	0.48	-0.15	31	27	41	34	66	2.9
DGE-8	0.36	0.74	0.49	-0.14	37	29	34	37	63	2.9
DGO-5	0.31	0.68	0.46	-0.17	26	28	45	40	60	3
DGO-6	0.29	0.73	0.40	-0.23	29	23	48	42	58	2
DGO-7	0.59	0.58	1.01	0.38	26	29	44	34	66	4
DGO-8	0.29	0.66	0.44	-0.19	31	13	55	31	69	2
DGO-11	0.42	0.65	0.65	0.02	24	29	47	42	58	3.2
DGO-14	0.27	0.69	0.39	-0.24	25	29	45	49	51	2.8
DGO-15	0.1	0.50	0.20	-0.43	22	40	38	56	44	5.3
Udachnaya Kimberlite (Kang *et al.*, 2019)										
U-400	0.18	0.57	0.32	-0.31	45	21	34	44	56	5
U-401	0.32	0.67	0.48	-0.15	32	34	33	18	82	5
U-402	0.36	0.39	0.93	0.30	18	12	69	15	85	5
Slave Craton (Brooker *et al.* 2024 & references therein)										
MX158	0.52	0.68	0.76	0.13	15	13	71	7	89	6.8
MX5001	0.12	0.51	0.24	-0.39	13	14	73	5	93	6.2
DDM_149	0.16	0.44	0.36	-0.27	13	11	76	14	84	5.7
DDM_327	0	0.36	0.00	-0.63	13	12	75	11	87	6.6
DDM_335	0.09	0.42	0.22	-0.41	11	15	73	10	87	6.3
DDM_360	0.08	0.39	0.20	-0.43	12	12	76	11	88	5.8
DDM_361	0.42	0.41	1.03	0.40	11	18	70	9	88	
DDM_368	0.1	0.48	0.21	-0.42	12	15	72	10	88	5.9
Hannouba Basaltic Plateau, China (Dai *et al.*, 2020)										
DMP441-PY	0.22	0.55	0.40	-0.23	14	11	74	15	85	1.51
DMP464-PV	0.44	0.35	1.25	0.62	10	11	78	16	84	1.26
Dabie-Sulu Orogen (Wang *et al.*, 2019)										
BXL-1	0.15	1.40	0.11	-0.52	37	21	42	40	56	3
BXL-4	0.62	1.54	0.40	-0.23	57	23	19	30	55	3
BXL-6	0.81	1.51	0.54	-0.09	57	23	19	32	53	3
HA-3	0.78	1.55	0.50	-0.13	65	27	8	40	50	1.7
HA-4	0.8	1.71	0.47	-0.16	63	30	5	40	52	1.7
SH-1	0.51	1.05	0.49	-0.14	54	26	19	42	54	2.8
SH-5	0.48	1.05	0.46	-0.17	58	24	17	35	58	2.8
ZMF-2	0.66	0.80	0.82	0.19	21	12	65	12	88	4.9
ZMF-3	0.64	0.95	0.67	0.04	21	12	66	5	95	4.9

Table S-7 continued.

Sample	measured $\Delta^{44/40}Ca_{grt\text{-}cpx}$	$10^6/T^2$	measured $\Delta^{44/40}Ca_{grt\text{-}cpx}$ / 106/T2	Residual: (measured $\Delta^{44/40}Ca_{grt\text{-}cpx}$ / $10^6/T^2$) - (predicted $\Delta^{44/40}Ca_{grt\text{-}cpx}$ at $10^6/T^2$ =1)	almandine content	grossular content	pyrope content	jadeite content	diopside content	literature pressure estimate (GPa)
Premier Kimberlite (Tappe *et al.*, 2021)										
CIM15-003	0.33	0.23	1.40	0.77	10	12	77	3	97	5.2
CIM15-021	0.11	0.27	0.40	-0.23	11	12	76	3	97	5.5
CIM15-022	0.34	0.25	1.35	0.72	12	11	76	3	97	5.3
CIM15-035	0.35	0.47	0.74	0.11	13	16	70	2	98	4.8
CIM15-040	0.92	0.79	1.16	0.53	14	12	74	0	100	2.8

7. Tests for Disequilibrium

To assess equilibrium, the garnet-clinopyroxene partitioning of Mg and Ti were compared to expected equilibrium values suggested by O'Reilly and Griffin (1995), and REE partitioning was compared with predictions from Sun and Liang (2015). The plots are included (Fig. S-6). Clinopyroxene and garnet Mg# are well correlated, and the average D_{Ti} is ~0.85, close to the expected value of ~1 (O'Reilly and Griffin, 1995). Additionally, the REE partitioning equilibrium was tested using the spreadsheet of Sun and Liang (2015) and the literature samples are broadly consistent with chemical equilibrium (two typical examples shown for samples from Bellsbank and Slave Craton). For NVF samples, Sun and Liang (2015) criteria could not be used since the jadeite content is too high, but the clinopyroxene-garnet REE partitioning (Fig. S-7) is similar to that expected for equilibrium (Green *et al.*, 2000).

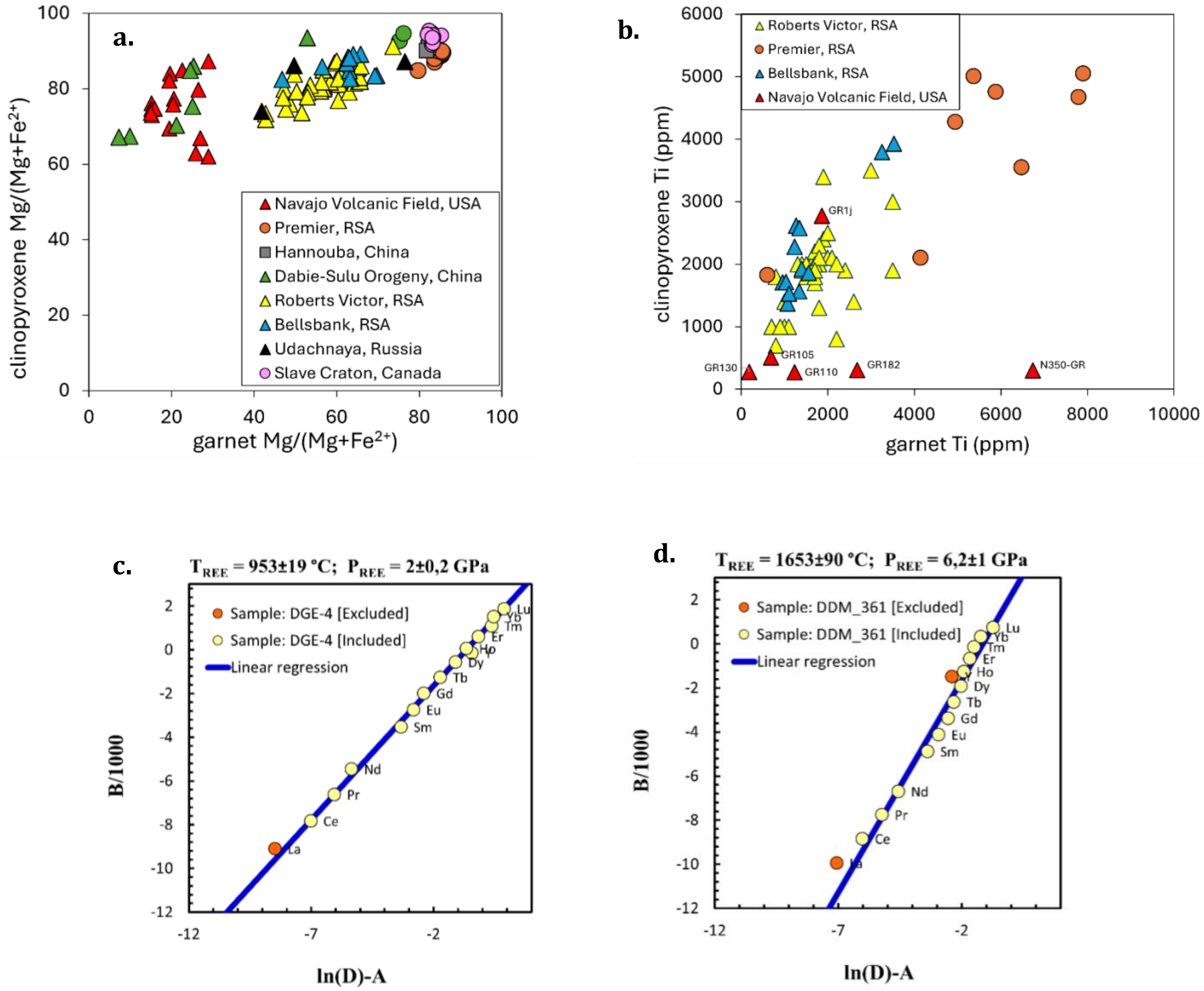

Figure S-6 Testing for disequilibrium in NVF sample and literature xenoliths with garnet versus clinopyroxene, a. Mg#, b. Ti, and REE partitioning in c. Bellsbank sample DGE-4 and d. Slave Craton sample DDM-361.

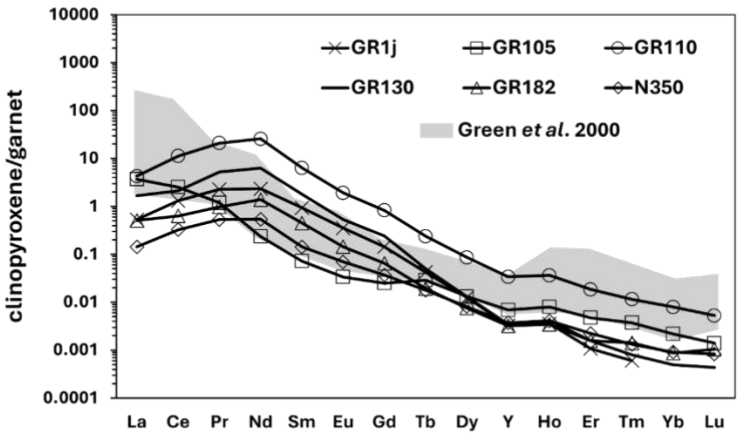

Figure S-7 Testing for disequilibrium in NVF sample, comparing clinopyroxene-garnet REE partitioning to experiments.

8. Regressions and Statistics

Below are the maximum likelihood linear regression results from Isoplot (Figure 1 data)

All data:

$\Delta^{44/40}Ca_{grt\text{-}cpx}$ = 1.44 (± 0.15) x $10^6/T^2$ – 0.51 (± 0.09), MSWD = 7.5, n=65 (Eq. S-1)

Excluding Roberts Victor Type II samples:

$\Delta^{44/40}Ca_{grt\text{-}cpx}$ = 0.96 (± 0.11) x $10^6/T^2$ – 0.22 (± 0.07), MSWD = 6.4, n=58 (Eq. S-2)

Excluding Dabie-Sulu and Roberts Victor Type II samples:

$\Delta^{44/40}Ca_{grt\text{-}cpx}$ = 1.09 (± 0.14) x $10^6/T^2$ – 0.28 (± 0.08), MSWD = 5.7, n=49 (Eq. S-3)

Below are the maximum likelihood linear regression results from Isoplot for Figure 1 with the intercept set at (0,0)

All data:

$\Delta^{44/40}Ca_{grt\text{-}cpx}$ = 0.61 (± 0.02) x $10^6/T^2$, MSWD = 11, n=65 (Eq. S-4)

Excluding Roberts Victor Type II samples:

$\Delta^{44/40}Ca_{grt\text{-}cpx}$ = 0.62 (± 0.02) x $10^6/T^2$, MSWD = 7.2, n=58 (Eq. S-5)

Excluding Dabie-Sulu and Roberts Victor Type II samples:

$\Delta^{44/40}Ca_{grt\text{-}cpx}$ = 0.63 (± 0.03) x $10^6/T^2$, MSWD = 6.8, n=49 (Eq. S-6)

Since equilibrium for Roberts Victor Type II eclogites is debated, they were excluded. Dabie-Sulu was then excluded since there is expected to be a $T_{Mg\text{-}Fe}$ and T_{Ca} mismatch. Eq. 2 is based on Eq. S-6 above and is the equation used or shown in each figure.

If the intercept is fixed at zero, the slope remains nearly unchanged regardless of whether the Dabie Sulu and Roberts Victor samples are excluded, indicating that consistency with theory does not depend on removing these data. The MSWD, though, improves significantly from 11 to 6.8, but is still quite far from the desired MSWD of 1. Hence, the Ca fractionation is not perfectly explained by the $1/T^2$ term (MSWD = 1), but rather there is still statistically significant scatter with MSWD of 6.8.

Statistics

Figure 1

x-axis ($10^6/T^2$): standard error (SE) is found by assuming that thermometry has an error of +/- 50 °C or higher (see Table S-5), and applying equations below. 2 standard errors (2SE) are shown in the figure (simply 2 x SE).

Left-side standard error = $10^6/T^2 - 10^6/(T+50\ °C)^2$ (Eq. S-7)

Right-side standard error = $10^6/(T-50\ °C)^2 - 10^6/T^2$ (Eq. S-8)

y-axis (measured $\Delta^{44/40}Ca_{grt\text{-}cpx}$): standard error (2SE) is calculated using: $SE_{\Delta Ca} = \sqrt{(SE_{\delta Ca\text{-}cpx}{}^2 + SE_{\delta Ca\text{-}grt}{}^2)}$ (Eq. S-9), where SE_{δ} is the standard error of each mineral measurement. $SE_{\delta Ca\text{-}cpx}$ and $SE_{\delta Ca\text{-}grt}$ were assumed to each be equivalent to the average standard errors of standards run in each study (e.g. BHVO-2, IAPSO, or BCR-2). Hence, if IAPSO was analysed with samples and yielded a 2SE of 0.09, then $SE_{\delta Ca\text{-}IAPSO} = SE_{\delta Ca\text{-}cpx} = SE_{\delta Ca\text{-}grt} = 0.09$ ‰. If the internal 2SE from a sample run is greater than the standard 2SE (here, 0.09‰), that larger 2SE is used for that mineral in Eq. S-10 above. Standard deviations (σ) are converted to SE with the relationship σ = standard error • √n (Eq. S-10), where necessary. 2 standard errors (2SE) are shown in the figure.

Figure 2

Expected error is presented as the normal distribution curve, centred at the mean of the residuals (-0.04) and 2σ = 0.14 ‰. The 2σ includes the propagated error from isotopic measurement $\Delta^{44/40}Ca_{grt\text{-}cpx}$, the error envelope from the linear regression Eq. 2 and $10^6/T^2$ estimate uncertainty: $\sigma_{expected} = \sqrt{(\sigma_{measurement}{}^2 + \sigma_{temp\ estimate}{}^2 + \sigma_{error\ envelope}{}^2)}$ (Eq. S-11).

Figure S-5

x-axis (measured $\Delta^{44/40}Ca_{grt\text{-}cpx}$): same as above for y-axis of Figure 1

y-axis (predicted $\Delta^{44/40}Ca_{grt\text{-}cpx}$): predicted $\Delta^{44/40}Ca_{grt\text{-}cpx}$ values were determined from the regression equation, hence their error is derived from $10^6/T^2$. 2SE for predicted $\Delta^{44/40}Ca_{grt\text{-}cpx}$ values are calculated as 0.63 x 2SE of $10^6/T^2$.

Supplementary Information References

Brooker, S.E., Barnes, J.D., Lassiter, J.C., Satkoski, A., Pearson, D.G. (2024) Tracking subduction-related metasomatism of the subcontinental lithospheric mantle using Ca-, O-, and H-isotopes. *Geochimica et Cosmochimica Acta* 385, 16–33. https://doi.org/10.1016/j.gca.2024.09.036

Chen, C., Huang, J.-X., Foley, S.F., Wang, Z., Moynier, F., Liu, Y., Dai, W., Li, M. (2020) Compositional and pressure controls on calcium and magnesium isotope fractionation in magmatic systems. *Geochimica et Cosmochimica Acta* 290, 257–270. https://doi.org/10.1016/j.gca.2020.09.006

Dai, W., Wang, Z., Liu, Y., Chen, C., Zong, K., Zhou, L., Zhang, G., Li, M., Moynier, F., Hu, Z. (2020) Calcium isotope compositions of mantle pyroxenites. *Geochimica et Cosmochimica Acta* 270, 144–159. https://doi.org/10.1016/j.gca.2019.11.024

Droop, G.T.R. (1987) A general equation for estimating Fe^{3+} concentrations in ferromagnesian silicates and oxides from microprobe analyses, using stoichiometric criteria. *Mineralogical Magazine* 51, 431–435. https://doi.org/10.1180/minmag.1987.051.361.10

Ellis, D.J., Green, D.H. (1979) An experimental study of the effect of Ca upon garnet-clinopyroxene Fe-Mg exchange equilibria. *Contributions to Mineralogy and Petrology* 71, 13–22. https://doi.org/10.1007/BF00371878

Gréau, Y., Huang, J.-X., Griffin, W.L., Renac, C., Alard, O., O'Reilly, S.Y. (2011) Type I eclogites from Roberts Victor kimberlites: Products of extensive mantle metasomatism. *Geochimica et Cosmochimica Acta* 75, 6927–6954. https://doi.org/10.1016/j.gca.2011.08.035

Green, T.H., Blundy, J.D., Adam, J., Yaxley, G.M. (2000) SIMS determination of trace element partition coefficients between garnet, clinopyroxene and hydrous basaltic liquids at 2–7.5 GPa and 1080–1200°C. *Lithos* 53, 165–187. https://doi.org/10.1016/S0024-4937(00)00023-2

Helmstaedt, H., Doig, R. (1975) Eclogite nodules from kimberlite pipes of the Colorado plateau—samples of subducted Franciscan-type oceanic lithosphere. *Physics and Chemistry of the Earth* 9, 95–111. https://doi.org/10.1016/0079-1946(75)90010-5

Hoover, W.F., Page, F.Z., Schulze, D.J., Kitajima, K., Valley, J.W. (2020) Massive Fluid Influx beneath the Colorado Plateau (USA) Related to Slab Removal and Diatreme Emplacement: Evidence from Oxygen Isotope Zoning in Eclogite Xenoliths. *Journal of Petrology* 61, egaa102. https://doi.org/10.1093/petrology/egaa102

Huang, J.-X., Gréau, Y., Griffin, W.L., O'Reilly, S.Y., Pearson, N.J. (2012) Multi-stage origin of Roberts Victor eclogites: Progressive metasomatism and its isotopic effects. *Lithos* 142–143, 161–181. https://doi.org/10.1016/j.lithos.2012.03.002

Huang, S., Farkaš, J., Jacobsen, S.B. (2011) Stable calcium isotopic compositions of Hawaiian shield lavas: Evidence for recycling of ancient marine carbonates into the mantle. *Geochimica et Cosmochimica Acta* 75, 4987–4997. https://doi.org/10.1016/j.gca.2011.06.010

Kang, J.-T., Ionov, D.A., Zhu, H.-L., Liu, F., Zhang, Z.-F., Liu, Z., Huang, F. (2019) Calcium isotope sources and fractionation during melt-rock interaction in the lithospheric mantle: Evidence from pyroxenites, wehrlites, and eclogites. *Chemical Geology* 524, 272–282. https://doi.org/10.1016/j.chemgeo.2019.06.010

Köhler, T.P., Brey, G.P. (1990) Calcium exchange between olivine and clinopyroxene calibrated as a geothermobarometer for natural peridotites from 2 to 60 kb with applications. *Geochimica et Cosmochimica Acta*, 54, 2375–2388. https://doi.org/10.1016/0016-7037(90)90226-B

Krogh, E.J. (1988) The garnet-clinopyroxene Fe-Mg geothermometer — a reinterpretation of existing experimental data. *Contributions to Mineralogy and Petrology* 99, 44–48.

Krogh Ravna, E.J., Paquin, J. (2003) Thermobarometric methodologies applicable to eclogites and garnet ultrabasites. In: Carswell, D.A., Compagnoni, R., Rolfo, F. (Eds.) *Ultrahigh Pressure Metamorphism*. Eötvös University Press, Budapest, 229–259. https://doi.org/10.1180/EMU-notes.5.8

Li, Y., Wu, Z., Huang, S., Wang, W. (2022) Pressure and concentration effects on intermineral calcium isotope fractionation involving garnet. *Chemical Geology* 591, 120722. https://doi.org/10.1016/j.chemgeo.2022.120722

O'Reilly, S.Y., Griffin, W.L. (1995) Trace-element partitioning between garnet and clinopyroxene in mantle-derived pyroxenites and eclogites: *P-T-X* controls. *Chemical Geology* 121, 105–130. https://doi.org/10.1016/0009-2541(94)00147-Z

Powell, R. (1985) Regression diagnostics and robust regression in geothermometer/geobarometer calibration: the garnet-clinopyroxene geothermometer revisited. *Journal of Metamorphic Geology* 3, 231–243. https://doi.org/10.1111/j.1525-1314.1985.tb00319.x

Ravna, K. (2000) The garnet–clinopyroxene Fe^{2+}–Mg geothermometer: an updated calibration. *Journal of Metamorphic Geology* 18, 211–219. https://doi.org/10.1046/j.1525-1314.2000.00247.x

Roden, M.F., Smith, D., Murthy, V.R. (1990) Chemical constraints on lithosphere composition and evolution beneath the Colorado Plateau. *Journal of Geophysical Research: Solid Earth* 95, 2811–2831. https://doi.org/10.1029/JB095iB03p02811

Smart, K.A., Tappe, S., Woodland, A.B., Greyling, D.R., Harris, C., Gussone, N. (2021) Constraints on Archean crust recycling and the origin of mantle redox variability from the $\delta^{44/40}$Ca – δ^{18}O – fO_2 signatures of cratonic eclogites. *Earth and Planetary Science Letters* 556, 116720. https://doi.org/10.1016/j.epsl.2020.116720

Smith, D., Zientek, M. (1979) Mineral chemistry and zoning in eclogite inclusions from Colorado Plateau diatremes. *Contributions to Mineralogy and Petrology* 69, 119–131. https://doi.org/10.1007/BF00371855

Smith, D., Connelly, J.N., Manser, K., Moser, D.E., Housh, T.B., McDowell, F.W., Mack, L.E. (2004) Evolution of Navajo eclogites and hydration of the mantle wedge below the Colorado Plateau, southwestern United States. *Geochemistry, Geophysics, Geosystems* 5, Q04005. https://doi.org/10.1029/2003GC000675

Sudholz, Z.J., Green, D.H., Yaxley, G.M., Jaques, A.L. (2022) Mantle geothermometry: experimental evaluation and recalibration of Fe–Mg geothermometers for garnet-clinopyroxene and garnet-orthopyroxene in peridotite, pyroxenite and eclogite systems. *Contributions to Mineralogy and Petrology* 177, 77. https://doi.org/10.1007/s00410-022-01944-3

Sun, C., Liang, Y. (2015) A REE-in-garnet-clinopyroxene thermobarometer for eclogites, granulites and garnet peridotites. *Chemical Geology* 393–394, 79–92. https://doi.org/10.1016/j.chemgeo.2014.11.014

Tappe, S., Massuyeau, M., Smart, K.A., Woodland, A.B., Gussone, N., Milne, S., Stracke, A. (2021) Sheared Peridotite and Megacryst Formation Beneath the Kaapvaal Craton: a Snapshot of Tectonomagmatic Processes across the Lithosphere–Asthenosphere Transition. *Journal of Petrology* 62, egab046. https://doi.org/10.1093/petrology/egab046

Usui, T., Nakamura, E., Helmstaedt, H. (2006) Petrology and Geochemistry of Eclogite Xenoliths from the Colorado Plateau: Implications for the Evolution of Subducted Oceanic Crust. *Journal of Petrology* 47, 929–964. https://doi.org/10.1093/petrology/egi101

Wang, Y., He, Y., Wu, H., Zhu, C., Huang, S., Huang, J. (2019) Calcium isotope fractionation during crustal melting and magma differentiation: Granitoid and mineral-pair perspectives. *Geochimica et Cosmochimica Acta* 259, 37–52. https://doi.org/10.1016/j.gca.2019.05.030